Università degli Studi di Napoli Federico II
Ph.D. Program in
Information and Communication Technology for Health
XXXV Cycle

THESIS FOR THE DEGREE OF DOCTOR OF PHILOSOPHY

Visible light backscattering techniques for IoT healthcare applications

by
MUHAMMAD HABIB ULLAH

Advisor: Prof. Giacinto Gelli

Co-advisor: Prof. Francesco Verde

SCUOLA POLITECNICA E DELLE SCIENZE DI BASE
DIPARTIMENTO DI INGEGNERIA ELETTRICA E DELLE TECNOLOGIE DELL'INFORMAZIONE

Dedicated to my parents,
my loving wife
and my siblings.

Candidate's declaration

I hereby declare that this thesis submitted to obtain the academic degree of Philosophiæ Doctor (Ph.D.) in Information and Communication Technology for Health is my own unaided work, that I have not used other than the sources indicated, and that all direct and indirect sources are acknowledged as references.

Parts of this dissertation have been published in international journals and/or conference articles (see list of the author's publications at the end of the thesis).

Napoli, March 8, 2023

(Muhammad Habib Ullah)

Acknowledgments

First of all, I am grateful to the Almighty ALLAH for establishing me to complete this work.

I place on record my sincere gratitude and thanks to my research supervisor, Prof. Giacinto Gelli, for his persistent support, continuous guidance, and invaluable advice during my Ph.D. study. His rigorous professional attitude toward novel scientific research and his approach to solve complex problems have helped me in my research. Without his suggestions, encouragement, patience, and conscientiousness, I would not be able to successfully complete this dissertation. It has been a great pleasure for me to have him as my supervisor.

I would also thank Prof. Francesco Verde for his valuable advices and guidance. I have learned very useful lessons from his research and industrial experience. His ideas, cooperation and discussions have helped me alot to achieve good results.

I am pleased to acknowledge Dr. Amir Masood Khalid, for his assistance and helpful discussions.

Last but not the least, I would like to express my deepest gratitude to my family. Thanks for their generous and endless love to me. They are always with me when I go through tough situations and provide encouragement and support to me. Without their support, this research work would not happen.

Contents

List of Figures

List of Tables

Introduction

Rapid advances in the field of information and communication technology (ICT) are replacing traditional healthcare systems with *electronic health* (e-Health) ones. Many e-Health applications involve the use of sensors of different nature, aimed at collecting physiological parameters of the patients and transmitting them in real-time to a collection units. *Radio-frequency* (RF) technologies are frequently employed to this aim, notwithstanding their drawbacks, such as long-term exposure to RF fields, which might be a source of health risks and electromagnetic interference (EMI) to medical equipments, as well as security of privacy concerns, due to RF propagation behind walls and obstacles. Moreover, because of spectrum shortage, RF technologies exhibit serious scalability issues to support the massive number of connections required by the Internet of Things (IoT) vision.

Visible light backscattering (or backscatter) (VLB) is an innovative optical transmission paradigm aimed at enabling ultra low-power passive communication and localization for IoT, which overcomes some of the known limitations of conventional (i.e., active) *visible light communication* (VLC), as well as those of active/passive RF technologies. Indeed, VLB can be considered as an evolution of VLC, which leverage the diffusion of *light emitting diodes* (LEDs) to jointly provide illumination and communication to multiple tags, using *visible light* (VL) in the range of wavelengths from 390 to 720 nm. VLB employs the principle of optical *backscattering* (BS), which allows a device to perform passive communication by reflecting a portion of the incoming energy, with very little energy consumption.

Due to complexity and energy constraints, VLB schemes employ simple devices and modulation formats, aimed at supporting low-rate transmission, in the order of some kilobits per second. VLB solves the limitations of conventional VLC by providing a low-energy, low-rate communication link, which also solves the scalability issues inherent to RF communications. Indeed, VLB techniques might represent a viable solution in many different healthcare setups, including operating and emergency rooms, intensive care units, imaging and pathology labs, and hospital wards.

A number of VLBC techniques have been recently proposed, and some proposals to use them in healthcare are considered in the literature. However, most contributions are mainly experimental in nature, and several theoretical issues, mainly regarding link modeling, signal and noise characterization, performance analysis, channel estimation and equalization, are usually lacking. In this thesis, we aim at filling the aforementioned gaps, and establish a solid ground to VLB research, by considering some fundamental theoretical issues and deriving simple yet accurate mathematical models, which are further corroborated by computer simulation results. Moreover, at the end of our analysis, we delineate some promising directions for future VLB research activities.

This thesis is structured as follows. **Chapter 1** introduces the VLB principles and describe the state-of-the-art and applications of VLB, with particular reference to IoT domains. In **Chapter 2**, the VLB link is modeled and the performance analysis of a VLB communication technique is derived and corroborated by numerical simulations. **Chapter 3** presents channel estimation and equalization techniques for VLB communication systems, whose performances are analyzed by Monte Carlo computer simulations. Future promising research directions are delineated in **Chapter 4**.

The research presented in this dissertation has been supported by the Italian Ministry of University and Research (MUR). The author's work has been partially carried out in the framework of the REPBAN (**RE**flected-**P**ower **B**ody **A**rea **N**etworks) project at the Department of Electrical Engineering and Information Technologies (DIETI).

Chapter 1

Visible light backscattering

In this Chapter,[1] we provide a comprehensive survey of current research activities on visible light backscattering (VLB) systems, which leverage backscatter principles in the optical domain to perform data communication and/or localization. After describing the principles of operation of VLB and the main enabling technologies, we classify existing VLB techniques according to several features, discussing their merits and limitations. Moreover, we introduce the potential applications of VLB techniques in several IoT domains.

1.1 Introduction

The adoption of radio-frequency (RF) communication technologies to support large-scale connectivity for the Internet of Things (IoT) exhibits severe scalability issues, related to energy constraints, as well as spectral efficiency limitations and RF spectrum congestion (so called "spectrum crunch"). Another drawback of RF communications is the leakage through walls and obstacles, which not only complicates interference management, but also poses serious security and privacy concerns. Moreover, in some scenarios, such as aircraft/spaceship cabins and hospitals, or hazardous environments, such as

---

[1] The content of this Chapter is mainly based on References 1 and 3 of the Author's publication list.

chemical or nuclear plants and oil ducts, usage of RF technologies must be limited or completely avoided.

To cope with the aforementioned drawbacks, a viable solution is to employ *visible light communication* (VLC) techniques [1], which work in the portion of the wavelength spectrum that is visible to human eyes (from about 400 nm to 700 nm), offering a huge unlicensed bandwidth for the potential support of a massive number of IoT nodes. The key idea of VLC is to jointly carry illumination and data, by modulating the light emitted by *light emitting diodes* (LEDs), which allows one to reuse the existing lighting infrastructure for communication or localization.

In a typical VLC deployment, a LED, connected to the data network infrastructure via a wired/wireless link, performs downlink (DL) transmission to one or multiple client devices. Several types of modulations, starting from the base *on-off keying* (OOK), can be superimposed on lighting, provided that the switching frequency is large enough to avoid an annoying *flickering* effect.

Visible light (VL) can also be used for localization purposes, leading thus to *visible light positioning* (VLP) systems [2, 3, 4, 5, 6, 7, 8, 9], which can easily achieve centimeter-level accuracy. A VLP system operating indoors typically comprises several LED sources, acting as reference nodes or *anchors*, each one transmitting a VL signal to a *target* node, using one of different multiplexing protocols, such as *time-division multiplexing* (TDD) or *frequency-division multiplexing* (FDD). The transmitted VL signals convey data related to the anchors, such as their identity, coordinates, timestamps, and the transmitted power, which are needed to perform positioning. The target node decodes the data and measures some position-related parameters of the received signals, such as the *received signal strength* (RSS), *time-of-arrival* (TOA), *time-difference-of-arrival* (TDOA), or *angle-of-arrival* (AOA) [4]. Finally, the target node determines its own position (so called *client-based* localization) by using both the decoded data and the measured parameters, adopting algorithms such as proximity, fingerprinting, trilateration, multilateration, or triangulation [3].

In IoT applications, VL-based techniques offer several advantages over RF ones. However, a fundamental limitation of existing VL-based techniques is their inherent *one-directional* DL transmission (from the LED to the devices), usually lacking a return channel for uplink (UL) [10]. A common workaround is to employ RF technologies in UL, which however requires availability of RF spectrum and must cope with the aforementioned scalability issues. A more interesting solution would be to adopt optical communications also for UL transmission, such as, e.g., VLC itself, infrared (IR) or near-ultraviolet (near-UV), which however requires the integration of a power-hungry active light source (a LED or a laser) in the client devices. Similar limitations affect VLP systems, forcing them to resort to client-based localization (i.e., made by the target nodes). This could represent a bottleneck in large-scale IoT applications, where device capabilities are limited and it is thus desirable to transfer the heavy computational burden of real-time positioning and tracking to the anchor nodes, so called *server-based* positioning.

To overcome such limitations of *active* VLC and VLP systems, many recent papers have resorted to *visible light backscattering communications* (VLBC) for ultra low-power *passive* communication and localization. The backscatter (BS) paradigm has been first proposed for RF communications, allowing a device to transmit data by reflecting towards the source, after modulating it, a portion of the received electromagnetic field. Systems based on RF backscattering have been designed for the purposes of communication, identification, or localization, the most popular one being *radio-frequency identification* (RFID) [11]. A recent evolution of RF BS is *ambient backscatter* [12, 13, 14, 15] wherein passive communication leverages existing RF signals (such as, e.g., cellular, TV, or WiFi ones) without requiring dedicated illuminators.

1.2 VLB principles

VLB-based systems can be classified as *visible light backscatter communications* (VLBC) ones, targeted at data communications, and *visible light backscatter positioning* (VLBP) ones, aimed at localization purposes. In a

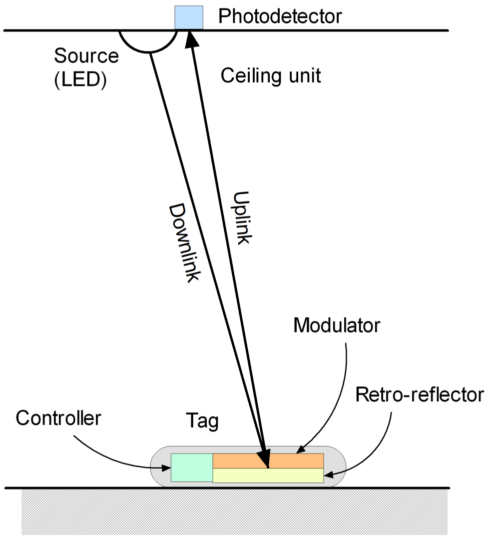

Figure 1.1: A pictorial view of a point-to-point VLBC system.

VLBC system, light is typically used for both DL and UL communications. In the simplest point-to-point scenario of Fig. 1.1, a LED acts both as light source and active DL transmitter (TX), while a device (called a "tag"), equipped with a *retroreflector* (see Section 1.3), performs passive UL transmission by reflecting the light, after modulating it, back towards the source. A variant of these scheme, referred to as *ambient light* or *sunlight BS communication*, assume that the light source cannot be controlled nor used for DL data transmission, which occurs either when artificial sources (e.g., LED bulbs) are used only for illumination, or when natural light sources (e.g., the sun) are exploited. In this case, communication is inherently one-directional (i.e., restricted to UL).

In many VLBC schemes, optical modulation at the tag is usually performed by means of simple *LCD shutter* devices (see Sec. 1.3). Due to power and complexity constraints, very simple *intensity* modulations, such as OOK, are generally employed in UL, whereas DL transmission could employ more sophisticated spectrally-efficient modulations [16]. Cheap photodiodes (PDs) are used at the receiver (RX) for signal detection both in DL and UL, even though more expensive *imaging* sensors, such as cameras, can be employed.

Differently from client-based VLP systems, where the target node carries the heavy burden of localization, in VLBP systems localization is usually performed by the transmitting LEDs on the basis of some measured parameters (such as RSS, TOA, TDOA, or AOA) together with some information backscattered by the tag itself, such as the tag identity, timestamps, or the transmitted power. Such VLBP systems are generally used indoors, where the GPS signal is often not available. Most VLBP systems assume that the tag can modify (by modulating it) in some way the light it receives, in order to leverage the localization task. A different approach is *device-free localization* [7], where the position of a target is determined by measuring its modifications to the light impinging on it, but without assuming that the target can intentionally modify the properties of light (this approach is sometimes referred to as *passive localization*).

One distinct advantage of VL-based positioning techniques over active/passive RF-based ones, such as RFID, WiFi, Bluetooth or ultra-wideband (UWB) ones, is the high localization accuracy attainable and the lack of the need to install a dedicated infrastructure, since they can leverage the existing lighting systems. Moreover, compared specifically with WiFi-based positioning, the number of LED luminaries and their power is generally much higher than that of WiFi access points [1]. Finally, different from conventional VLP systems, the presence of a return (UL) channel in VLBP systems allows one to implement not only client-based localization techniques, but also server-based ones, paving also the way for cooperative/collaborative localization systems [17, 18], where the target nodes exchange information via VLB links to ease the localization task.

1.3 VLB-enabling technologies

In this Section, we describe two main enabling technologies for VLB systems: *retroreflectors* and *LCD shutters*.

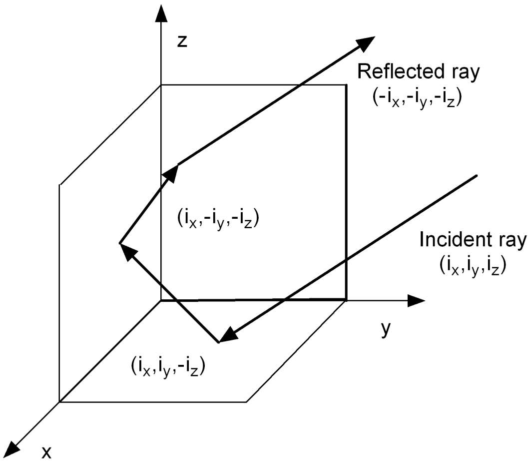

Figure 1.2: Working principle of a CCRR based on ray optics.

Retroreflectors

An optical retroreflector (RR) is a device that, unlike a mirror, reflects the incident light back towards the direction of the source, with minimal scattering. RRs can be implemented with different technologies and are used in many fields, including free-space optical communications networks [19, 20, 21], satellite communications [22], and low-powered sensor networks [23, 24, 25].Cheap RR materials are commonly available (e.g., Scotchlite™ manufactured by 3M) and are used for road signs, bicycles, and clothing for road safety [26].

One popular type of RR is the *corner-cube retroreflector* (CCRR) [27], which is composed by three mirrors arranged in a 90 ° corner geometry. Light rays are sent back towards the source regardless of the relative orientation of the incoming beam direction, after undergoing three reflections, as depicted in Fig. 1.2. Another common type of RR is the *spherical retroreflector* (commony known as “cat’s eyes”), which is build as a high index-of-refraction transparent sphere with a reflective backing [28]. A less common implementation is is the *phase-conjugate mirror* [29], which exploits nonlinear optics phenomena such as four-wave mixing or stimulated Brillouin scattering. It is worth noting that innovative materials such as *metasurfaces* can also be used as RRs, as further discussed in Section 4.3.

Disregarding the actual implementation, it is common to describe [28] the behavior of a RR device by means of two angles (Fig. 1.3): the *entrance angle* β, which is the angle between the illumination direction and the normal to the RR surface, and the *observation angle* α, which is the angle between the illumination direction and the viewing direction. High-quality retroreflectors work over fairly wide entrance angles, up to $45°$ or more (up to $90°$ for pavement marking), with very small observation angles ($< 1°$).

The performance of RRs can be measured by several coefficients, the most common ones [28] are R_I and R_A. The first one is the *coefficient of retroreflected luminous intensity:*

$$R_I = \frac{I}{E_\perp} \qquad \text{[cd/lux]} \tag{1.1}$$

where $E_\perp$ is the illuminance (in lux) on a plane normal to the direction of illumination, and I is the intensity (in cd) of the illuminating light. The second one is the *coefficient of retroreflection*:

$$R_A = \frac{I}{E_\perp A} = \frac{R_I}{A} \qquad \text{[(cd/m}^2\text{)/lux]} \tag{1.2}$$

where A is the area of the retroreflector. Values for RA of several hundred (cd/m^2)/lux are not uncommon [28]. Both coefficients are functions of the angles β and α.

Finally, it should be noted that RRs can also be used as optical modulators, by controlling the reflection mechanisms with *micro-electromechanical systems* (MEMS) [21] or semiconductor *multiple quantum wells* (MQW) technologies [26].

LCD shutters

LCD shutters are employed in consumer 3D TV glasses [30] and act as modulator devices in most VLBC protoypes. An LCD shutter is characterized by a

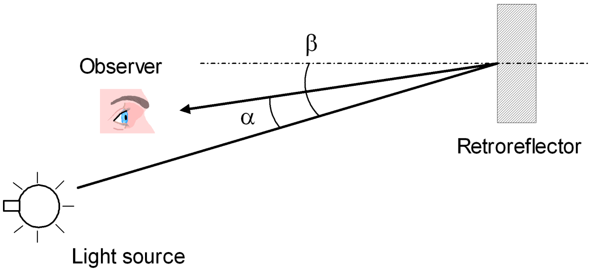

Figure 1.3: Geometrical description of a RR: β is the entrance angle, α is the observation angle.

multilayer sandwich structure [31], with two linear polarizers at the ends and one *liquid crystal* (LC) layer in between.[2] Each polarizer obeys the *Malus law:*

$$I_\theta = I_0 \cos^2\theta \tag{1.3}$$

where I_0 is the intensity of light impinging on the polarizer, I_θ is the intensity of light that is passed through the polarizer, and θ is the angle between the polarization direction of the polarizer and the polarization of light. If the polarization of the incident light is parallel to that of the polarizer, i.e., $\theta = 0°$, no attenuation will occur and the light will pass unaltered through the polarizer. When, instead, the two directions are perpendicular, i.e., $\theta = 90°$, the entire incident light is blocked by the polarizer.

Modulation of bits in a LCD shutter is based on polarization properties of light. In Fig. 1.4, the working principle of a *twisted nematic* (TN) LCD shutter is explained [32]. A variable voltage is applied between the layers of a TN LC, which determines a twist/untwist (realignment) of the LC molecules. In most commodity TN LCs, when no voltage is applied (normal or uncharged state), a light beam passing through the LC layer undergoes a rotation by $90°$. Thus, polarizer 2 can entirely block the light if placed parallel to the incident

---

[2] A liquid crystal (LC) is a special material whose properties are between those of a liquid and those of a crystal. The most common type of LC is a *nematic* liquid crystal, whose optical behavior can be modified by applying an electric field to it.

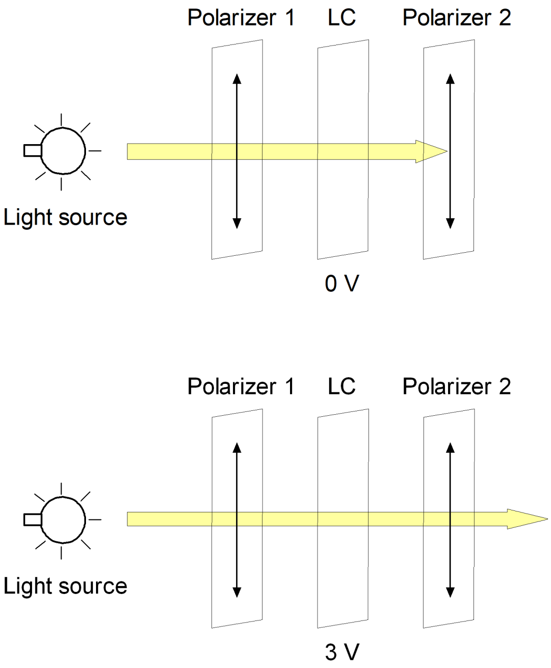

Figure 1.4: An LCD shutter operating as an OOK modulator. When no voltage is applied to the LC (top), the polarization of the light is rotated by 90 degrees and is blocked by the second polarizer. When a certain voltage (3 V) is applied to the LC (bottom), the polarization of the light is not rotated and passes trough the second polarizer.

light. Therefore, when the voltage is increased, untwisting of LC molecules will happen and polarizer 2 will become brighter. Over a certain voltage level, such as 3 V, complete untwisting of LC molecules occurs (charged state) and this result in the brightest state of polarizer 2. Hence, the intensity of the light can be modulated by tuning the applied voltage so as to encode bits using bright and dark states.[3]

The most interesting features of LCD shutters are, among others, compatibility with non-coherent white light [34], low power consumption (sub-mW

---

[3] Some LCD shutters employ orthogonal polarizers at the two ends [33], in which case the encoding of voltage levels to bright/dark states is simply reversed.

[26]) and low cost (0.03 \$ per cm^2 [35]).

However, the achievable data-rate is restricted due to asymmetric and slow impulse response of the LCD shutters[30, 33].This thing also complicates equalization and reduces data rate to sub-kbps level.The rising time of 1.096 ms and a falling time of 0.533 ms have been reported by [30], whereas in [33] the corresponding values of 0.3 ms and 4 ms were found. The falling time is much larger than the rising time and it is caused by slow discharging property.

A simplified model for the response of the LCD shutter is that of a first-order RC filter with a cutoff frequency in the order of 300 Hz [30]. However, LCD shutters exhibit an asymmetric response and a marked nonlinear behavior [36, 33], which make them very difficult to generate multilevel modulated signals [26]. Finally, the slow switching rate of LCD shutters might induce flickering.

1.4 Existing VLB techniques

In this Section, a survey of the existing VLBC techniques is provided, whose main features are also summarized in Tab 1.1. The techniques are presented mainly in chronological order.

Retro-VLC [31]

This bi-directional VLBC system performs DL transmission by employing conventional VLC techniques, whereas UL transmission is based on VLBC. The UL TX employs a RR device coupled with an LCD shutter as modulator. Several power optimization solutions are proposed, together with an implementation based on purely analog techniques to reduce energy consumption at the tag. The Retro-VLC prototype employs Manchester-encoded binary signals, achieving a data-rate of 10 kbps in DL and 0.5 kbps in UL over a range of 2.4 m in an office environment.

Ambient light BS communication [30]

This VLBC system exploits either ambient light or a dedicated illuminator for UL transmission. The design is similar to [31] and the developed prototype achieves a data-rate of 100 bps over a 10 cm range in a typical office environment.

MobileVLC [37, 38]

In the VLBC system for UL communications (later referred to as *MobileVLC*) proposed in [37], information is statically encoded in a tag composed by a reflective surface. Such a surface is mounted on a mobile object (like a car or truck), and can be read by illuminating it with an unmodulated source (artificial or natural) and detecting the reflected light with a PD-based RX. The system works similarly to a bar-code reader, but without using energy-consuming cameras for reading, since the power consumed by the PD is very low (about 1.5 mW). One possible improvement of MobileVLC is the dynamic encoding of data, which can be performed by adopting advanced materials or devices (such as e-ink screens, LCD shutters, or metasurfaces) whose reflection properties can be adjusted in real-time. Further studies and optimizations [38] allow one to improve the performance of MobileVLC, by increasing data-rate, range, and mobile object speed, as well as improving robustness.

Pixelated VLC-backscatter [39]

The VLBC scheme proposed in [39] employs multilevel modulation to improve the data-rate of the simple OOK-based Retro-VLC technique [31]. Since the highly nonlinear characteristic of the LCD shutter prevents modulating a single LCD-shutter with more than two levels, the proposed solution employs *multiple* LCD shutters, whose number is equal to $\log_2(M)$ (with M denoting the cardinality) of the modulation, which are independently switched by the modulation bits. A RR and a LCD shutter form a *pixel* that can be switched independently from the others. Hence, the overall reflected light is proportional to the number of activated pixels, which allows one to obtain multilevel pulse amplitude modulation (PAM) signals. The prototype in [39] employs up to three pixels and works at the symbol rate of 200 symbols/s, implementing OOK, 4-PAM, and 8-PAM modulations, with an achieved throughput of 600 b/s at 2 m, 400 b/s at 3 m, and 200 b/s at 5 m. Rate adaptation should be performed, where lower-order and more robust modulations, such as OOK, are used when the range is higher and viceversa. A possible improvement to this scheme, mentioned by the same authors, is the adoption of orthogonal frequency-division multiplexing (OFDM) modulation techniques.

PassiveVLC [26]

The technique proposed in [26] tries to improve the design of Retro-VLC [31] by specifically focusing on the modulation/coding schemes. In particular, to solve the problem of long consecutive stream of zeros/ones, it is proposed to replace the meoryless Manchester coding scheme employed in [31] with the Miller one, due to its better spectral efficiency. The choice of a modulation scheme with memory slightly complicates the decoding algorithm, which can be formulated as an optimization problem and solved by means of dynamic programming methods.

Another innovation of the PassiveVLC technique is avoiding to completely charge/discharge the LCD shutter, in order to reduce the switching time (from 4 ms down to 1 ms). The resulting solution is called *trend-based modulation* (TBM), since the information is mapped on the "trend" of the voltage change, avoiding hence the slower complete charge/discharge, at the price of a reduced immunity to noise. The PassiveVLC prototype achieves up to 1 kbps in UL over 1 m for a flexible range of orientations and different ambient light conditions.

RetroArray [40]

This technique exploits the nonlinear behavior of the LCD shutter to improve the data-rate of existing VLBC systems. Indeed, LCD shutters exhibit an highly asymmetric response, with 0.5 and 4 ms charging and discharging time, respectively. The RetroArray prototype employs an array of LCD shutters and encodes the information only on the rising (i.e., charging) edges, resorting to time interleaving between different shutters to achieve multilevel modulation. The technique, called *delayed superimposition modulation* (DSM), allows one to achieve an UL data-rate of 4 kbps over 3 m using an array of 16 LCD shutters.

Poster [34]

This VLBC scheme employs *polarization-based quadrature-amplitude modulation* (PQAM) to overcome the problem of flickering, associated to the low switching rate of the LCD shutter. Similarly to [35], the LCD TX employs only one polarizer, thus mapping the information on two orthogonal polarizations, which are controlled by the LC layer. This completely avoids flickering, since the intensity of the backscattered light is not changed. At the RX, a second polarizer is capable of detecting the different polarizations. The PQAM design is robust to the cases where TX and RX are not perfectly aligned, in terms of polarization angle.

Sunlight BS communications [41, 42, 43, 44]

The research works belonging to this class are oriented to the use of natural light sources, such as sunlight, for VLBC. This scenario has some specific issues, since it works outdoors with no control on the source, and is restricted to UL transmissions. Moreover, the presence of clouds might severely affect the availability and characteristics of the link. Differently from of Fig. 1.1, where light source and PD are co-located, in sunlight-based communications they are obviously placed at different locations. One advantage of this approach is the high illumination that can be obtained with sunlight (of the order of tens of thousands of lux), which paves the way for potentially very high-rate/high-range transmissions.

One of the pioneering contributions in this area is the aforementioned MobileVLC system [37], which can work both indoors (with artificial light) and outdoors (with artificial light or sunlight).

LuxLink [41] works with any ambient light source (either artificial one or sunlight) and adopts *frequency-shift keying* (FSK) modulation to avoid flickering. It achieves a very low data-rate (80 bps) at ranges of 4 m indoors and 10–60 m outdoors. Another work in this area is ChromaLux [42], which exploits the *birefringence*[4] property, by stacking up to 6 LC shutters to increase the contrast without changing the transition period, which allows one to design particular constellations aimed at increasing the data-rate/range. The developed prototype works indoors with ambient light, reaching 1.55 kbps at 5 m and 1 kbps at 10 m, with BER values below 0.01.

PhotoLink [43] employs for BS transmission *digital micro-mirror devices* (DMDs), which are optical systems composed by a large number of highly-reflective microscopic mirrors (with linear dimension less than 10 μm each), whose orientation can be electrically controlled. They are typically used in consumer electronics to implement high-quality displays, but their control logic can be modified to make them act as high-speed optical modulators. The system proposed in [43] adopts flicker-free FSK modulation and achieves very high data-rates, up to 80 kbps outdoors working with sunlight.

Finally, SunBox [44] is a short-range (in the order of 10 cm) VLBC system employing artificial light or sunlight. The reflective device is a *smectic* LCoS (LC over silicon) microdisplay, consuming 110-180 mW, whereas a low-end smartphone camera (working at 30 FPS) acts as RX. By employing Reed-Solomon codes, the developed prototype achieves a variable throughput of 2–10 kbps, operating indoors with standard lighting, or outdoors with sunlight under different cloud conditions.

RetroI2V [45]

This system exploits retroreflective coating of the road signs for VLBC in outdoors scenarios. Late-polarization and polarization-based differential reception technique are used to mitigate flickering. Experimental results show that

---

[4] Birefringence is the optical property of certain non-isotropic materials, whose refractive index depends on the polarization and propagation direction of light.

the system exhibits long range (up to 100 m) connectivity. Efficient operation is achieved by using a decentralized multiple-access control (MAC) protocol. A limitation of this scheme is that it can be used only for one-way communication and it is designed for a specific vehicular application.

RetroTurbo [33]

A VLBC prototype is implemented in [33], which uses PQAM and DSM for IoT-oriented applications. It achieves an UL data-rate of 8 kbps at 7.5 m range, which is 32x higher than OOK [31]. The range increases to 10 m if the data-rate is decreased to 4 kbps. The Authors also designed a real-time demodulation algorithm and claimed a 128x rate gain (32 kbps) via emulation.

RETRO and PassiveRETRO [46, 47, 48]

In [46, 47, 48] several VLBP systems for server-based localization are proposed. The RETRO system [46, 48] performs real-time tracking of location and orientation of passive IoT nodes equipped with a RR and an LCD shutter, which transmit their identity to the network. The prototype exploits received signal strength (RSS) measures and trilateration to achieve ultra low-power centimeter-level positioning.

An improvement is the RR-based PassiveRETRO system [47], which retains the advantages of RETRO [46, 48] but eliminates the LCD shutter at the tag. This design choice completely avoids the necessity of any electronic component on the IoT devices. Polarization-based modulation and bandpass optical filters are used as means to identify and separate the signals reflected by different IoT devices. Moreover, *optical rotatory dispersion*[5] is used for mitigating interchannel interference and improving signal-to-interference-plus-noise ratio (SINR) for each node. Specifically, the PassiveRETRO system splits the LCD shutter present in RETRO into two parts: one linear polarizer and one LC layer are installed on the light source for performing polarization-

---

[5] Optical rotatory dispersion is a property of some materials that rotate the polarization of light to different extents depending on the wavelength.

based modulation, while another linear polarizer is placed on top of the RR to modulate the backscattered light.

RetroMUMIMO [49]

To support low-latency concurrent transmissions, the RetroMUMIMO system [49] exploits the different shapes of the pulses emitted by LCD shutters (due to changes in position, orientation, manufacturing, etc.), so called *pulse diversity*, as well as conventional RX diversity, The transmission of up to 8 tags is modeled as a MIMO-like problem, where demodulation is based on maximum-likelihood (ML) decoding, whose complexity is reduced by a preliminary pulse feature extraction and dimensionality-reduction technique based on singular value decomposition (SVD). A larger number of tags is accommodated by means of a centralized, slotted, and contention-based MAC protocol. The power consumption of the tag is 0.2 mW during transmission, and the testbed achieves concurrent transmission of 8 tags, each transmitting at 800 bps in a typical indoor environment with different ambient light conditions.

The testbed is robust to ambient light and to the near-far effect, supporting the given rate with BER values less than 0.01 at 2.50 m for 8 tags, at 3.25 m for 6 tags, and at 3.75 m for 4 tags. Moreover, extensive simulations are reported to benchmark the proposed system in different operative simulations, in comparison with the RetroTurbo [33] system, showing a marked reduction of the network latency and a good scalability of latency performance with the number of tags.

RetroFlex [50]

This system performs bi-directional VLBC-based communication with robots, leveraging the properties of *polymer dispersed liquid crystal* (PDLC) technology to implement VLB modulation, and using a smartphone both as a source light (flashlight) and RX (camera). The flexible nature of PDLCs make them readily deployable on irregular surfaces, such as those of robots. An array of 4 PDLCs is used to encode the information to be transmitted in UL. The system achieves up to 60 bps at 2.5 m with a view angle of 70° in several lighting conditions, ranging from day light to artificial light. The power consumption of the tag is around 18 mW, and the UL data-rate is mainly limited by the camera frame-rate, as typically occurs in camera-based RXs.

Scheme	**Technology**	**Light source**	**Modulation**	**UL data-rate [bps]**	**Range [m]**	**Tag power consumption**	**Main advantages**	**Main limitations**
Retro-VLC [31]	RR + LCD shutter	LED	OOK w/ Manchester coding	500	2.4	234 μW	Bidirectional, low-power, analog implementation	Low data-rate, narrow FoV
Ambient light BS communication [30]	RR + LCD shutter	LED/ambient light	OOK	100	0.1	N/A	Ambient light source or dedicated illuminator	Low data-rate, low-range
MobileVLC [37]	Reflective surface	Ambient light	OOK w/ Manchester coding	50	1	N/A	Ambient light source, mobile node	Very low data-rate, low-range, static encoding of information
Pixelated VLBC [39]	Multiple LCD shutters	LED	OOK, 4-PAM, 8-PAM	600	2	200 μW	High data-rate, rate adaptation	Complexity
PassiveVLC [26]	RR + LCD shutter	LED	TBM w/ Miller coding	1 000	1	150 μW	High data-rate, flexible range of orientations	Reduced immunity to noise
RetroArray [40]	Multiple LCD shutters	LED	DSM	4 000	3	N/A	High data-rate	Complexity
Poster [34]	RR + LCD shutter	LED	PQAM	N/A	2	N/A	Flicker-free, robust to TX/RX orientation	Complexity
LuxLink [41]	LCD shutter	Ambient light	FSK	80	4–60	$\sim$ 20–30 mW	Ambient light source, flicker-free	Low data-rate, narrow FoV
ChromaLux [42]	Multiple LCD shutters	Ambient light	Polarization-based	1 000	50	28 mW	Ambient light source, high data-rate, long-range, flicker-free	Sensitivity to LCD manufacturing inaccuracies
PhotoLink [43]	DMD	Ambient light	4-FSK	80 000	4	45 mW	Ambient light source, high data-rate	Cost
SunBox [44]	Smectic LCoS + camera RX	Ambient light	Polarization-based	10 000	0.1	110–180 mW	Ambient light source, high data-rate, flicker-free	Very short-range
RetroI2V [51]	Retroreflective coating	LED (headlight)	OOK	N/A	$\sim$ 100	$\sim$ 2–20 μJ/bit	Decentralized MAC protocol, flicker-free, long-range	One-way communication, only vehicular scenario
RetroTurbo [33]	Modified LCD	LED	PQAM + DSM	8 000	7.5	0.8 mW	High data-rate, real-time demodulation algorithm	Complexity
RETRO [46, 48]	RR + LCD shutter	LED	OOK	N/A	1.5	Ultra low-power	Centimeter-level positioning (based on RSS and trilateration)	N/A
PassiveRETRO [47]	RR + linear polarizer	LED	PQAM	N/A	1	Ultra low-power	Mitigation of interchannel interference, completely passive tag	RX complexity
RetroMUMIMO [49]	LCD shutter	LED	OOK with pulse diversity	800	2.50	0.2 mW	Scalable, low-latency, near-far resistant	RX complexity
RetroFlex [50]	Multiple PDLCs + camera RX	LED (flashlight)	OOK	60	2.5	18 mW	Flexible tag, wide FoV	Low data-rate

Table 1.1: A summary of existing VLB techniques.

1.5 Main applications of VLB in IoT domains

VLB techniques can be employed in several IoT domains, mainly to supplement or replace VLC and/or RF technologies when extreme energy efficiency is pursued. In the following, some fields of application are discussed.

Healthcare

In e-Health and m-Health applications [52, 53], sensors of different nature are used to monitor some physiological parameters of the patients (such as, e.g., temperature, pulse, blood pressure, or oxygen saturation) and transmit them in real-time to a collection unit. The use of RF communication technologies to this aim presents two main drawbacks: (i) long-term overexposure to RF fields, which amplifies the risks to human health; (ii) electromagnetic interference (EMI), which affects the accuracy and reliability of medical equipments.

Optical-based VLC and VLB techniques allows one to overcome the previous drawbacks, and can be used in many different healthcare setups, including operating and emergency rooms, intensive care units, imaging and pathology labs, and hospital wards. In particular, the use of VLBC techniques is particularly appealing in *wireless body area networks* (WBANs) [54], composed by wearable or textile sensors aimed at long-term health monitoring. Indeed, WBAN must inherently adopt energy-efficient devices and protocols for sensing and communication. Moreover, wearable devices are equipped with low-capacity batteries, whose recharging or substitution might be cumbersome.

Application of a VLB-based technique to an hospital ward scenario is depicted in Fig. 1.5. In this scenario, data communication is performed using the IoT device or transceiver placed at the wrist or shoulder of the patient. A ceiling unit consisting of a LED transmitter and a PD receiver is connected to the Internet or a private network infrastructure. The IoT device (tag) at the patient side consists of a RR, LCD shutter and controller. In UL, VLBC is employed to transmit towards the ceiling unit the data gathered by the sensors placed on the body of the patient.

In [55], a VLBC system for health monitoring applications is studied,

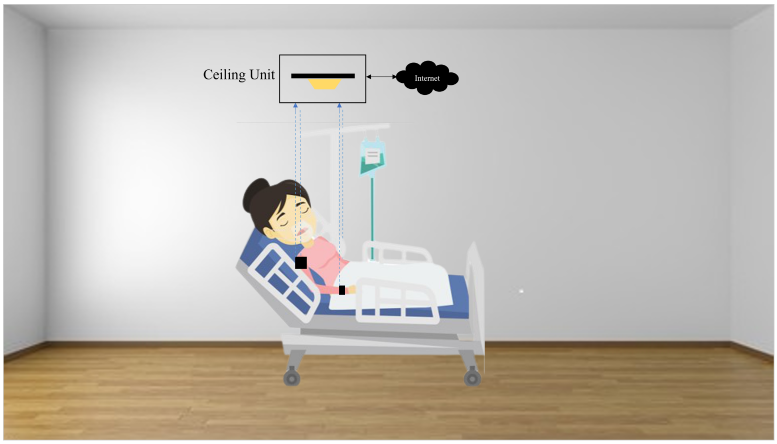

Figure 1.5: Patient monitoring scenario in an hospital ward.

which exploits the light emitted by a LED to transmit, by means of a CCRR, OOK-modulated data acquired by wearable sensors to a central unit. The RX at the ceiling employs an imaging sensor to detect the transmitted data. A link budget analysis is proposed, aimed at assessing the theoretical performances of the system, in terms of BER, achievable range, and data-rate. This solution is further generalized in [56, 57] to an *hybrid* system providing two different operation modes: an *active* one based on IR and a *passive* one employing VLBC. The active mode is used when VLBC cannot be used, that is, when the LED light is turned off or the user is too far from the source.

Transportations

Intelligent transportation systems (ITSs) are critical components to make transport safer, more efficient, more reliable, and more sustainable. They make widespread use of IoT technologies to enable automated collection of transportation data and information exchange between vehicles/passengers and infrastructures.

Recently, VLC techniques have been proposed to replace RF ones in *vehicle-to-vehicle* (V2V), *vehicle-to-infrastructure* (V2I), and *infrastructure-to-vehicle* (I2V) links, (see [58] and references therein). Their use relies on the ubiquitous availability of LED-based street, traffic and vehicle lights. A distinctive feature of VLC-based vehicular communications is the outdoor operating scenario, characterized by a non-negligible ambient light interference due to background solar radiation. As discussed in Section 2.3, this type of interference can adversely affect the reliability of VLC and VLB techniques, unless suitable mitigation strategies are performed.

The VLBC system called RetroI2V [45] assures flicker-free I2V data transmission over distances of about 100 m, under different lighting conditions. It works by equipping the road signs with tiles of transparent LCD shutters plus controling/harvesting circuitry, actually converting conventional road signs into smart, dynamic transmitters. Several usage scenarios are discussed in [45], aimed at providing additional information to drivers (i.e., possible accidents or time restrictions) or adapting the messages to road/weather conditions.

Notwithstanding the successful demonstration of [45], we do not envision VLB as a candidate technology for outdoors mission-critical applications, such as autonomous driving or collision avoidance systems. VLB can be used instead to transmit or share low-rate information, such as traffic or road conditions, points-of-interest, or travel suggestions. in non-critical infotainment applications. Other areas where VLB technologies can be fruitfully used is in automatic toll or ticketing systems, to provide information about free parking lots, or as support to green shared-mobility systems, such as bikesharing or scooter sharing systems.

We envisage that VLB technologies are more useful in public transportation systems working in indoor scenarios, such as galleries or metro railway stations, or to provide low-rate communications within vehicles. For example, VLB can be used to provide indoor localization when GPS is absent, or to assist precise stop control of train vehicles to platforms. Another application of is substitution of RF techniques in smart ticketing and access control systems. Moreover, VLB technologies can be used also to support more innovative functions, such as counting people to implement crowd-avoiding functionalities in ITSs [59].

Smart cities

The wide availability of outdoor lightning infrastructures in urban environments is a formidable enabler for VLC and VLB applications. Moreover, adoption of VLB-based sensing and communications can avoid to further congestionate the RF spectrum in urban environments. Possible application of interest could be, for instance, in smart parking (detection of free spaces in parking lots), environmental sensing (i.e., for pollution checking) and cultural heritage. To enable long-range communications, it is envisioned that unmanned autonomous vehicles (UAVs) can be used to relay the information gathered by VLB sensors to a central unit [60].

Smart home

IR-based device control is common in consumer electronics and equipment: however, IR devices are subject to annoying battery replacement. Since homes and offices are equipped with LED luminaries, IR active devices can be easily replaced by passive VLB system, which assure long times of operation with a limited energy consumption.

Moreover, the indoor positioning capabilities of VLB make it the natural candidate for *home robotics* applications [61] (vacuum cleaners, monitoring devices, lawn mowers, etc.). Other natural applications are in smart lightning systems, where many small inexpensive VLB sensors are deployed in several points of the room to measure the light intensity and report the results to the lightning infrastructures. Moreover, VLB technologies can also be employed in security and anti-introsion systems, as well as into systems devoted to energy efficiency [62].

Logistics and industry

Wireless technologies, such as RFID and wireless sensor networks, are among the important enabling technologies for *smart logistics* [63] and *industrial IoT (IIoT)* [64]. Due to the already mentioned limitations, RF technologies can be conveniently replaced by VLC and VLB ones in several applications within this domains.

A promising use of VLB is that of indoor localization and identification of goods in retailers, shopping malls, and supermarkets, as a replacement of RFID or traditional bar codes. An example is the VLB technique proposed in [37], aimed at replacing RFID systems by encoding the information in a reflective surface, which is read by using only ambient illumination (i.e., the sun). More generally, the indoor localization capabilities of VLB can be applied in several industrial and logistics fields, such as real-time location of assets in a facility, i.e., tracking of vehicles in industrial sites or goods in retail shops. Triangulation-based VLB techniques based on TOA, TDOA, or RSSI [46, 47, 48] can be used to this aim. Thanks to the small wavelength of visible light, these techniques can easily achieve sub-meter or even centimeter-level accuracy. In robotics, VLB can be used to provide precise positioning and navigation aids in indoor environments.

Finally, VLBC techniques can also be used in hazardous environments, such as, e.g., petrochemical plants, oil ducts, or nuclear plants, where usage of RF technologies must be limited of avoided at all. VLBC techniques can be used for sensing and monitoring of indoor infrastructures such as galleries, ducts, pipelines, etc.

Chapter 2

VLB link modeling and performance analysis

In this Chapter,[1] we address the problem of characterizing the VLB link and assessing the performance of a VLBC system. Specifically, we develop a mathematical model of the VLB link, which allows one to accurately predict the amount of light required to ensure an acceptable received power. Moreover, we analytically show the impact of the relevant system parameters on the achievable bit-error-rate (BER) performance of the information transfer process, which highlights most vividly the interplay among the main system parameters, such as the end-to-end channel gain, the average transmitted optical power, and the power spectral density (PSD) of noise sources. Finally, we verify our analytical findings regarding system performance via numerical simulations.

2.1 VLC link modeling

Link modeling for optical wireless communications has been carried out in several papers, both for indoor and outdoor scenarios [65], especially for the IR region of the electromagnetic spectrum [66, 67]. In the following, we focus on

---

[1] The content of this Chapter is mainly based on Reference 2 of the Author's publication list.

indoor scenarios, which are in our opinion the most appealing ones for VLBC techniques; for the characterization of outdoor optical wireless channels we directly refer to [65].

The channel characteristics of an optical wireless link are fixed for a given position of the source, tag, and surrounding reflecting objects, changing only when these components are moved by distances in the order of centimeters [66]. Due to high bit rates and the relatively slow movement of objects and people within a room, the optical wireless channel typically varies only on a time scale of many bit periods and, hence, it may be considered as *quasi-static* [68].

Wireless optical propagation links can be classified according to the degree of directionality of source and tag, and the existence of a *line-of-sight* (LOS) path between them [69]. *Directed* links employ sources and tags with narrow radiation and illumination patterns, respectively, which have to be aligned in order to minimize path loss effects and reception of ambient light noise. On the other hand, *nondirected* links employ wide-angle sources and tags, which do not require such an accurate alignment. *Hybrid* links are also possible, which combine sources and tags having different degrees of directionality. The presence of a LOS path between the source and the tag allows link designs with maximum power efficiency and minimum multipath distortion. For LOS links, reflections are negligible and, consequently, the path loss is easily calculated from the knowledge of the transmitter beam divergence, receiver size, and separation distance between the source and the tag [66].

Non-line-of-sight (NLOS) links – also referred to as *diffuse* links – generally rely upon reflection of the light from the ceiling or some other diffusely reflecting surface, such as people or cubicle partitions, standing between the source and the tag. Compared to their LOS counterparts, as far as coverage is concerned, NLOS link designs ensure greatest robustness and ease of use. However, NLOS links, particularly in indoor applications, are subject to the effects of multipath propagation, similarly to RF systems. Multipath propagation causes the received signal to suffer from severe amplitude fades on the scale of a wavelength. However, optical receivers are typically equipped with large-area PDs, whose surface area is orders of magnitude larger than the transmission wavelength. In this case, the total photocurrent generated at the receiver is proportional to the integral of the optical power over such a large surface, thus providing an inherent spatial diversity that averages out fading effects [66]. Although indoor NLOS links are inherently robust against the effects of multipath fading, they suffer from the effects of multipath-induced dispersion, which causes *intersymbol interference* (ISI), thus adversely affecting link performance.

Several experimental channel characterizations have been carried out [70, 71, 72, 73, 74, 75], by considering both LOS and NLOS configurations. Results have shown that the optical channel response is sensitive not only to the position of the PD, but also to its orientation and rotation. Different models have been proposed, e.g., ceiling bounce [76], Hayasaka-Ito [77], and spherical [78], which are however targeted at the IR region.

2.2 VLB link modeling

Compared with its VLC counterpart, characterization of the VLB link is less explored, and many papers consider only experimental results without performing detailed analytical studies. In [46], a VLBC-based localization system has been proposed and a characterization of the RR has been provided. In [79], the link budget for a VLBC system has been derived, and a detailed simulation-based analysis of the signal-to-noise ratio (SNR) of the VLBC system has been provided. However, neither of the two contributions provides a detailed signal and noise characterization. Moreover, [79] does not provide a bit-error rate (BER) analysis of the OOK link.

A simple model for VLB links has been recently developed by us in [80] and will be presented in Section 2.3. Compared to [46] and [79], such a physics-based model provides interesting additional insights. However, further results regarding channel characterization for VLB applications are still needed.

There are three key issues that are relevant for VLB channel modeling:

reflection patterns of the RR, duplexing techniques, and noise characterization which will be discussed in the following sections.

Reflection patterns

Besides the presence of obstacles between the LED and the tag, which might absorb some power while scattering the rest, the VLB channel heavily depends on the reflection characteristics of the RR located at the tag. The reflection pattern of the RR can be approximated by using the *Lambert model* [67]. With reference to Fig. 1.1, according to Lambert model, the shape of the reflection pattern depends on the observation angle α. This fact allows to develop simple reflection models, which are easy to implement via software. However, the model of Lambert does not accurately approximate the reflection pattern of the RR around the specular reflection direction.

Phong [81] developed a reflection model, mostly adopted in computer graphics, employing both the entrance angle β and the observation angle α. The diffuse and specular components are suitably weighted by a modeling parameter $0 < r < 1$, which can be fitted to the RR characteristics. The *Phong model* is more complex than the Lambertian one and subsumes the latter as a special case when $r = 0$. Existing validations of the Phong's model mainly consider IR applications (see, e.g., [82]).

Duplexing

The bi-directional communication system of Fig. 1.1 can be further classified according to the connectivity between the LED and the tag. The possible connections are termed *half-duplex*, *out-of-band full-duplex*, and *in-band full-duplex*. The half-duplex connection is a VLB link whereby DL and UL transmissions cannot be made simultaneously. This can be implemented by resorting to TDD, according to which UL and DL transmissions are separated in time [80]. In the case of TDD, during the UL phase, the LED does not transmit data, thus acting as a conventional monochromatic illuminator.

The LED and the tag operate in out-of-band full-duplex when they transmit and receive over different VL bands. An innovative solution for implementing out-of-band full-duplex VLB systems is represented by the use of time-varying metasurfaces (see Section 4.3), which could enable the implementation of a FDD connection, where DL and UL transmissions proceed simultaneously over non-overlapping VL bands. In this case, VLB channel models have not been developed yet.

In-band full-duplex operation enables the LED to transmit and receive simultaneously over the same frequency band, hence improving throughput and reducing latency. A compact and flexible solution for implementing an in-band full-duplex VLB system might consist of replacing the LED and the photodetector in Fig. 1.1 with a single multiple-quantum-well (MQW) diode [83]. When approximately biased, the MQW-diode emits a broad spectrum of light. As a dual-functioning device, the MQW-diode also acts as a PD that absorbs photons to liberate electron-hole pairs. In this case, with respect to TDD/FDD, the UL channel model is more complicated.

Shot noise

VL indoor transceivers are subject to intense *ambient light*, emanating from both natural and artificial sources. The main sources of ambient light are the sunlight, incandescent lamps, and fluorescent lamps [84, 85, 86, 87]. The DC background photocurrent generated by the ambient light acts as a noise source in the receiver, referred to as *shot noise*, which degrades the link performance.

The sunlight is typically the strongest source of shot noise and represents an unmodulated source of the ambient light with a very wide spectral width and a maximum power spectral density (PSD) located at about 500 nm. The background current due to artificial illumination is only a few tens of μA, which is well below that produced by sunlight, which could be as high as 5 mA [84].

Besides ambient light, the performances of VLB systems are also adversely affected by the inherent *auto-interference* at the PD, which receives in UL both the BS signal from the tag and the light emitted by the LED to illuminate the tag. Such an auto-interference yields a photocurrent shot noise that, unlike ambient light, may be modeled as a non-stationary random process. Specifically, the auto-interference has a constant intensity in the TDD case, while it exhibits a time-varying intensity in the case of full-duplex connections. When FDD is employed, interference effects can be effectively reduced by using linear time-invariant (LTI) filtering techniques. On the other hand, in the case of in-band full-duplex communications, more advanced interference cancellation techniques have to be employed. In the simplest cases, to mitigate such a phenomenon, some form of physical shielding can be used [31].

2.3 The proposed VLBC link model

Our link model is aimed at describing the bi-directional VLBC system of Fig. 1.1, where a LED transmits in DL a modulated signal to the tag, whereas for UL transmission the tag modulates and reflects the light received by the LED. Both the tag and LED are equipped for reception by an *optical filter* (OF), a *nonimaging concentrator* (NIC), and a PD, followed by electrical processing of the converted signal.

In our analysis, we assume that the distance d between the LED and the tag is much larger than the size of the tag, so that all the incident rays on both LED and tag can be considered as parallel with the same angle [46]. Moreover, we assume that both DL and UL propagations are directed LOS, neglecting any ambient reflections. In the following subsections, with reference to the geometry of Fig. 2.1, we introduce path loss models for both DL and UL.

DL link model

Let $\overline{P}_{\text{tx,led}}$ denote the average optical power transmitted by the LED, the *irradiance* (W/m^2) at the tag is given [66] by

$$I_{\text{tag}}(\theta) = \frac{\overline{P}_{\text{tx,led}}\, R_{\text{led}}(\theta)}{d^2} \tag{2.1}$$

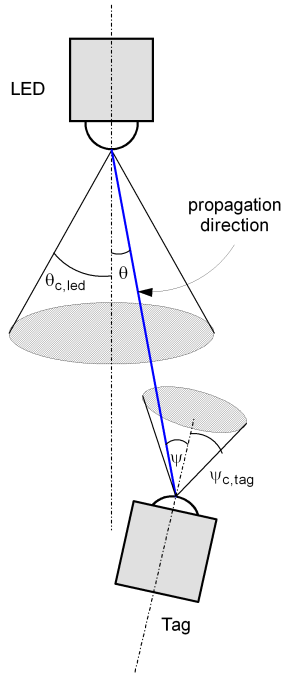

Figure 2.1: VLBC geometry for optical channel modeling.

where $\theta \in (-\pi/2, \pi/2)$ is the irradiation angle (see Fig. 2.1) and $R_{\text{led}}(\theta)$ is the LED radiation pattern, which is normalized so that $2\pi \int_0^{\pi/2} R_{\text{led}}(\theta)\, \sin(\theta)\, d\theta = 1$.

A reasonable model for LED source radiation is the *generalized Lambertian* one [66], according to which the normalized radiation pattern is given by

$$R_{\text{led}}(\theta) = \frac{(m+1)}{2\pi} \cos^m(\theta) \tag{2.2}$$

where m is the Lambertian order, which is related on the transmitter semi-angle $\theta_{1/2}$ at half-power, i.e., the solution of the equation $R_{\text{led}}(\theta) = R_{\text{led}}(0)/2$, as follows

$$m = -\frac{\ln(2)}{\ln \cos(\theta_{1/2})} \, . \tag{2.3}$$

For example, $\theta_{\frac{1}{2}} = 60^\circ$ (Lambertian transmitter) corresponds to $m = 1$, while

$\theta_{\frac{1}{2}} = 15°$ (directional transmitter) corresponds to $m \approx 20$.

The average optical received power $P_{\text{rx,tag}}$ (in W) at the tag is thus given by

$$\overline{P}_{\text{rx,tag}} = I_{\text{tag}}(\theta)\, A_{\text{eff,tag}}(\psi) \tag{2.4}$$

where $A_{\text{eff,tag}}(\psi)$ is the *effective* area of the tag PD, which is related to its physical area A_{tag} by

$$A_{\text{eff,tag}}(\psi) = A_{\text{tag}}\, T_{\text{tag}}(\psi)\, G_{\text{tag}}(\psi)\, \cos(\psi) \tag{2.5}$$

where $\psi \in (-\pi/2, \pi/2)$ is the illumination angle, $T_{\text{tag}}(\psi)$ is the transmission function of the OF, and $g_{\text{tag}}(\psi)$ is the gain of the NIC. For an ideal NIC with an internal refractive index n_{tag}, the concentrator gain can be expressed as

$$G_{\text{tag}}(\psi) = \begin{cases} \dfrac{n_{\text{tag}}^2}{\sin^2 \psi_{c,\text{tag}}}, & 0 \leq \psi \leq \psi_{c,\text{tag}} \\ 0, & \psi > \psi_{c,\text{tag}} \end{cases} \tag{2.6}$$

where $\psi_{c,\text{tag}}$ is the NCI field of view (FOV) at the tag. Equation (2.6) shows that the concentrator gain increases when the FOV is reduced.

By substituting (2.1) into (2.4) and taking into account (2.2) and (2.5), one has

$$\overline{P}_{\text{rx,tag}} = \overline{P}_{\text{tx,led}}\, H_{\text{dl}}(0) \tag{2.7}$$

where $H_{\text{dl}}(0)$ is the downlink DC channel gain [66, 79], which is given by

$$H_{\text{dl}}(0) = \frac{(m+1)A_{\text{tag}}}{2\pi d^2} \cos^m(\theta)\, T_{\text{tag}}(\psi)\, G_{\text{tag}}(\psi)\, \cos(\psi)\,. \tag{2.8}$$

UL link model

Since UL communication is based on VLBC, the starting point of our analysis is the irradiance at the tag, given by (2.1). An ideal RR performs specular reflection in the direction of the source, hence the irradiance (W/m^2) at the

LED receiver is

$$I_{\text{led}}(\theta) = \frac{\overline{P}_{\text{tx,led}}\, R_{\text{led}}(\theta)\, R_{\text{retro}}(\theta)}{(2d)^2} \tag{2.9}$$

where $R_{\text{retro}}(\theta)$ is the RR efficiency in the direction θ, which also incorporates possible losses due to modulation at the tag, and the term $(2d)^2$ arises due to round-trip propagation [46].

The average optical received power $\overline{P}_{\text{rx,led}}$ at the LED receiver is hence given by

$$\overline{P}_{\text{rx,led}} = I_{\text{led}}(\theta)\, A_{\text{eff,led}}(\theta) \tag{2.10}$$

where $A_{\text{eff,led}}(\psi)$ is the effective area of the LED PD, which is related to its physical area A_{led} by a relation similar to (2.5):

$$A_{\text{eff,led}}(\theta) = A_{\text{led}}\, T_{\text{led}}(\theta)\, g_{\text{led}}(\theta)\, \cos(\theta) \tag{2.11}$$

where the transmission function of the OF is denoted by $T_{\text{led}}(\theta)$ and $G_{\text{led}}(\theta)$ is the gain of the NIC at the LED, which can be expressed for an ideal NIC as in (2.6), with obvious modifications.

By substituting (2.9) into (2.10), and taking into account (2.2) and (2.11), one has

$$\overline{P}_{\text{rx,led}} = \overline{P}_{\text{tx,led}}\, H_{\text{ul}}(0) \tag{2.12}$$

where $H_{\text{ul}}(0)$ is the uplink DC channel gain given by

$$H_{\text{ul}}(0) = \frac{(m+1) A_{\text{led}} R_{\text{retro}}}{8\pi d^2} \cos^{m+1}(\theta)\, T_{\text{led}}(\theta)\, G_{\text{led}}(\theta)\,. \tag{2.13}$$

It should be noted that the obtained path loss, similar to [46], obeys a $1/d^2$ law, whereas in [79] a $1/d^4$ law is predicted, which however has not been validated experimentally.

2.4 The proposed VLBC signal and noise model

In the following subsections, we introduce a simple signal-level model and discuss noise characterization. A more detailed signal model, oriented to packet transmission and incorporating the effects of the LCD shutter response, is presented in Chapter 3.

Signal model

With reference to DL, the current driving the LED source can be written as

$$s_{\text{dl}}(t) = I_{\text{bias}} + \sum_{\ell=0}^{K_{\text{dl}}-1} d[\ell]\, p_{\text{dl}}(t - \ell T_{\text{dl}}) \tag{2.14}$$

where $d[\ell]$ is the data sequence (of length K_{dl}) to be transmitted in DL, $p_{\text{dl}}(t)$ is the pulse waveform, T_{dl} is the symbol interval, and I_{bias} is the DC bias current needed for illumination. The signal (2.14) is subject to the constraint [88] that $s_{\text{dl}}(t)$ be real and non-negative (so called *intensity modulation*).

Assuming an ideal (i.e., linear) electrical-to-optical conversion, the instantaneous optical power emitted by the LED is

$$P_{\text{tx,led}}(t) = \mathcal{R}_{\text{led}}\, s_{\text{dl}}(t) \tag{2.15}$$

where $\mathcal{R}_{\text{led}}$ (W/A) is the LED *responsivity* [89]. Under LOS propagation, the received optical power at the tag is [66]

$$P_{\text{rx,tag}}(t) = \alpha_{\text{dl}}\, P_{\text{tx,led}}(t - \tau_{\text{dl}}) \tag{2.16}$$

where α_{dl} and τ_{dl} model DL attenuation and delay, respectively.

The signal to be transmitted by the tag in UL is

$$s_{\text{ul}}(t) = \sum_{\ell=0}^{K_{\text{ul}}-1} u[\ell]\, p_{\text{ul}}(t - \ell T_{\text{ul}}) \tag{2.17}$$

where $u[\ell]$ is the data sequence (of length K_{ul}) to be transmitted in UL, $p_{\text{ul}}(t)$ is the pulse waveform (possibly incorporating also the response of the modulator) and T_{ul} is the symbol interval. Since $s_{\text{ul}}(t)$ has to control the switching of the LCD shutter, it is also subject to the constraint that $s_{\text{ul}}(t)$ be real and non-negative.

Signal (2.17) is used to intensity-modulate the received optical signal, generating the instantaneous backscattered power:

$$P_{\text{bs,tag}}(t) = s_{\text{ul}}(t)\, P_{\text{rx,tag}}(t)\;. \tag{2.18}$$

Thus, the optical received power at the LED receiver is

$$P_{\text{rx,led}}(t) = \alpha_{\text{ul}}\, P_{\text{bs,tag}}(t-\tau_{\text{ul}}) \tag{2.19}$$

where α_{ul} and τ_{ul} model UL attenuation and delay, respectively.[2]

By taking into account (2.18) and (2.16), one has

$$\begin{align} P_{\text{rx,led}}(t) &= \alpha_{\text{ul}}\, s_{\text{ul}}(t-\tau_{\text{ul}})\, P_{\text{rx,tag}}(t-\tau_{\text{ul}}) \tag{2.20} \\ &= \alpha_{\text{ul}}\, \alpha_{\text{dl}}\, s_{\text{ul}}(t-\tau_{\text{ul}})\, P_{\text{tx,led}}(t-\tau_{\text{ul}}-\tau_{\text{dl}})\;. \tag{2.21} \end{align}$$

To simplify UL reception, we assume that the system employs TDD, i.e., UL and DL transmissions are separated in time. In this case, during the UL phase, $s_{\text{dl}}(t) = I_{\text{bias}}$ in (2.14), hence $P_{\text{tx,led}}(t) = P_{\text{tx,led}}$. With this simplification, one has

$$P_{\text{rx,led}}(t) = \alpha_{\text{ul}}\, \alpha_{\text{dl}}\, s_{\text{ul}}(t-\tau_{\text{ul}})\, P_{\text{tx,led}}\;. \tag{2.22}$$

Before proceeding further, we highlight that, by time and ensemble averaging (2.22), one has

$$\overline{P}_{\text{rx,led}} = \alpha_{\text{ul}}\, \alpha_{\text{dl}}\, \overline{s}_{\text{ul}}\, \overline{P}_{\text{tx,led}} \tag{2.23}$$

where $\overline{s}_{\text{ul}} \triangleq \langle E[s_{\text{ul}}(t)]\rangle$, with $\langle\cdot\rangle$ and $E[\cdot]$ denoting infinite-time averaging and ensemble averaging, respectively. By comparison with (2.12), it results that $\alpha_{\text{ul}}\, \alpha_{\text{dl}} \overline{s}_{\text{ul}} = H_{\text{ul}}(0)$, which allows one to rewrite (2.22) as

$$P_{\text{rx,led}}(t) = H_{\text{ul}}(0)\, \overline{s}_{\text{ul}}(t-\tau_{\text{ul}})\, P_{\text{tx,led}} \tag{2.24}$$

---

[2] We assume that there is enough shielding to isolate the received backscattered signal from the signal emitted by the source in DL [31].

where, with a slight abuse of notation, we have defined $\overline{s}_{\text{ul}}(t) \stackrel{\triangle}{=} s_{\text{ul}}(t)/\overline{s}_{\text{ul}}$.

At the LED receiver, the optical power given by (2.24) is converted into a current by the PD as follows:

$$i(t) = \mathcal{R}_{\text{pd}} P_{\text{rx,led}}(t) + i_{\text{n}}(t) \tag{2.25}$$

where $\mathcal{R}_{\text{pd}}$ (A/W) is the PD *responsivity* [89], and $i_{\text{n}}(t)$ takes into account all the noise sources (including shot noise and thermal noise) at the output of the PD. Signal (2.25) is further amplified and filtered, thus resulting in

$$\begin{aligned} r(t) = i(t) * h_{\text{rx}}(t) &= \mathcal{R}_{\text{pd}}\, P_{\text{rx,led}}(t) * h_{\text{rx}}(t) + i_{\text{n}}(t) * h_{\text{rx}}(t) \\ &= \mathcal{R}_{\text{pd}}\, H_{\text{ul}}(0)\, P_{\text{tx,led}}\, \overline{s}_{\text{ul}}(t-\tau_{\text{ul}}) * h_{\text{rx}}(t) + w(t) \end{aligned} \tag{2.26}$$

where the impulse response $h_{\text{rx}}(t)$ models the cascade of amplifier and filter, while $w(t) \stackrel{\triangle}{=} i_{\text{n}}(t) * h_{\text{rx}}(t)$ is the noise at the output of the filter, with $*$ denoting convolution.

By defining for convenience $\beta_{\text{ul}} \stackrel{\triangle}{=} \mathcal{R}_{\text{pd}}\, H_{\text{ul}}(0)\, P_{\text{tx,led}}/\overline{s}_{\text{ul}}$ and remembering the definition of $s_{\text{ul}}(t)$, we have the simplification

$$\begin{aligned} r(t) &= \beta_{\text{ul}}\, s_{\text{ul}}(t-\tau_{\text{ul}}) * h_{\text{rx}}(t) + w(t) \\ &= \sum_{\ell=-\infty}^{\infty} u[\ell]\, h_{\text{ul}}(t-\tau_{\text{ul}}-\ell\, T_{\text{ul}}) + w(t) \end{aligned} \tag{2.27}$$

where

$$h_{\text{ul}}(t) \stackrel{\triangle}{=} \beta_{\text{ul}}\, p_{\text{ul}}(t) * h_{\text{rx}}(t) \tag{2.28}$$

is the impulse response of the overall channel, incorporating the effects of the LCD pulse shutter waveform and of the RX filter.

Noise characterization

The term $i_{\text{n}}(t) = i_{\text{shot}}(t) + i_{\text{therm}}(t)$ in (2.25) comprises [90] the two primary sources of noise at the LED receiver, that is, *thermal noise* deriving from RX electronics and *shot noise* modeling fluctuations of the photocurrent around its average value. Shot noise depends on the desired light beam as well as on ambient background light. For a PIN PD [89], the one-sided PSD (A^2/Hz) can be written as

$$S_{\text{shot}}(f) = 2\,e\,[\mathcal{R}_{\text{pd}}\,P_{\text{rx,led}} + I_{\text{dark}} + I_{\text{back}}] \tag{2.29}$$

where $e = 1.60 \cdot 10^{-19}$ C is the elementary electron charge, I_{dark} is the dark current, and I_{back} is the background current [84] due to natural or artificial light sources. It should be noted that the shot noise PSD might vary with the signal level, since it depends on the received optical power $P_{\text{rx,led}}$.

The one-sided PSD (A^2/Hz) of thermal noise is [90]

$$S_{\text{therm}}(f) = \frac{4\,k_{\text{B}}\,T\,F_{\text{n}}}{R_{\text{L}}} \tag{2.30}$$

where $k_{\text{B}} = 1.38 \cdot 10^{-23}$ J/K is the Boltzmann constant, T is the temperature of the load resistor (usually assumed to be $T = 290$ K), R_{L} is the load resistance, and F_{n} is the noise figure of the front-end stage of the receiver.

Hereinafter, we approximate [90] the overall noise as a white Gaussian random process, whose one-sided PSD (A^2/Hz) is given by

$$N_0 \stackrel{\triangle}{=} 2\,e\,[\mathcal{R}_{\text{pd}}\,P_{\text{rx,led}} + I_{\text{dark}} + I_{\text{back}}] + \frac{4\,k_{\text{B}}\,T\,F_{\text{n}}}{R_{\text{L}}}\,. \tag{2.31}$$

2.5 Uplink BER performance analysis

In this Section, we perform theoretical evaluation of the BER in UL, which is considered as the main parameter to assess the quality of a digital communication link [91].

Optimal reception of a modulated signal corrupted by additive white Gaussian noise (AWGN) is based [91] on matched filtering, followed by T_{ul}-spaced sampling and threshold detector. In this case, $h_{\text{rx}}(t) = p_{\text{ul}}(-t)$ and thus equation (2.26) can be elaborated, by assuming $\tau_{\text{ul}} = 0$ for the sake of simplicity and recalling that $\beta_{\text{ul}} = \mathcal{R}_{\text{pd}} H_{\text{ul}}(0) P_{\text{tx,led}}/\overline{s}_{\text{ul}}$, as

$$r(t) = \beta_{\text{ul}} \sum_{\ell=0}^{K_{\text{ul}}-1} u[\ell]\, R_{\text{ul}}(t - \ell T_{\text{ul}}) + w(t) \tag{2.32}$$

where $w(t) \triangleq i_{\text{n}}(t) * h_{\text{rx}}(t) = i_{\text{n}}(t) * p_{\text{ul}}(-t)$ and, additionally, $R_{\text{ul}}(t) \triangleq p_{\text{ul}}(t) * p_{\text{ul}}(-t)$ denotes the autocorrelation function of the UL pulse. For the sake of simplicity, we assume in the following that $p_{\text{ul}}(t)$ is a NRZ rectangular waveform:[3]

$$p_{\text{ul}}(t) = \begin{cases} 1, & t \in (0, T_{\text{ul}})\,; \\ 0, & \text{otherwise.} \end{cases} \tag{2.33}$$

The received signal $r(t)$ is sampled at time epochs kT_{ul}, with $k \in \{0, 1, \ldots, K_{\text{ul}} - 1\}$, and, since there is no ISI, the signal statistic for demodulating $u[k]$ can be simply expressed as

$$r[k] = \beta_{\text{ul}}\, E_{\text{ul}}\, u[k] + w[k] \tag{2.34}$$

where $E_{\text{ul}} = \int_{-\infty}^{+\infty} p_{\text{ul}}^2(t)\, dt = T_{\text{ul}}$ is the pulse energy, and $w[k] \triangleq w(kT_{\text{ul}}) \sim \mathcal{N}(0, \sigma_w^2)$, with $\sigma_w^2 = (N_0/2)E_{\text{ul}}$, where N_0 is given by (2.31). Thus, it is straightforward to derive the BER expression by assuming ideal OOK with infinite *extinction ratio* [90], that is, $u(k) \in \{0, 1\}$ with equal probabilities. In this case one has:

$$r[k] = \begin{cases} \beta_{\text{ul}}\, E_{\text{ul}} + w[k], & u[k] = 1\,; \\ w[k], & u[k] = 0\,. \end{cases} \tag{2.35}$$

To detect $u[k]$, we compare $r[k]$ with the threshold r_{tresh}. It should be noted that, due to the presence of shot noise, the variance σ_w^2 is different when $u[k] =$

---

[3] A more realistic analysis, which takes into account the LCD shutter response, is carried out in Chapter 3.

0 or $u[k] = 1$, as reported in the following:

$$\sigma_w^2 = \begin{cases} (e(I_{\text{dark}} + I_{\text{back}}) + \frac{2k_B T F_n}{R_L})\, E_{\text{ul}} \triangleq \sigma_{w,0}^2 \,, & u[k] = 0 \,; \\ [e(\beta_{\text{ul}} + I_{\text{dark}} + I_{\text{back}}) + \frac{2k_B T F_n}{R_L}]\, E_{\text{ul}} \triangleq \sigma_{w,1}^2 \,, & u[k] = 1 \,. \end{cases} \tag{2.36}$$

The optimal threshold can be written [90] as

$$r_{\text{tresh}} = \frac{\sigma_{w,0}\, I_1}{\sigma_{w,0} + \sigma_{w,1}} \tag{2.37}$$

where $I_1 \triangleq \beta_{\text{ul}}\, E_{\text{ul}}$ and the resulting BER can be written as

$$\text{BER} = Q\left(\frac{I_1}{\sigma_{w,0} + \sigma_{w,1}}\right) \,. \tag{2.38}$$

By straightforward substitutions, it is possible to obtain an explicit but cumbersome expression of the BER as a function of all involved parameters. Note that, under our assumptions, the value of $\overline{s}_{\text{ul}}$ needed to evaluate β_{ul} turns out to be $1/2$.

2.6 Numerical results

In this section, numerical evaluation of the BER in UL is performed for a digital healthcare communication link. This link can be used to transmit data collected by sensors of different nature, used to monitor some physiological parameters of the patients (such as, e.g., temperature, pulse, blood pressure, or oxygen saturation). The required values of BER and data-rate for these services are in the range 10^{-3} to 10^{-10} and 20 b/s to 10 Mb/s, respectively [95, 96]. A comparison of BER performance of state-of-the-art VLC and VLBC systems is given in Tab. 2.1

We present numerical results of the proposed BER performance analysis for a VLBC system with one LED and one tag, employing OOK modulation in UL. A large room (typical of an hospital ward) with dimensions 8 m × 8 m × 4 m is considered, and the transmitting LED is placed at the center of the

Research article	Type of UL source	BER
[92]	active	$< 10^{-5}$
[93]	active	$< 3.8 \times 10^{-3}$
[94]	active	$< 1.5 \times 10^{-3}$
[56]	passive	$< 10^{-6}$
[39]	passive	10^{-3}
[79]	passive	10^{-3}

Table 2.1: Performance requirements of state-of-the-art VLC and VLBC links.

ceiling. The tag is placed at the receiver plane, which is parallel to the room floor, at an height of 0.5 m. The main simulation parameters are summarized in Tab. 2.2. The rationale behind the selection of the simulation parameters is the balance between accuracy and computational efficiency. Furthermore, we have selected specific simulation parameters by keeping in mind the specifications of PDs, RRs and OFs made by leading manufacturers of optical equipment, such as, Hamamatsu, Thorlabs, and Iridian [97, 98, 99, 100].

Parameters	Values
Room dimensions	8 m $\times$ 8 m $\times$ 4 m
Modulation scheme	OOK
Bit-rate	1 Mb/s
LED location	Center of the ceiling
Tag location	Variable in the room (height $= 0.5$ m)
RR efficiency (tag)	0.60
TX power (LED)	0.8 W
TX semi-angle (LED)	60°
FOV of concentrator (LED)	90°
PD area (LED)	50 mm^2
PD responsivity (LED)	0.4 A/W
OF gain (LED RX)	0.5
Load resistor (LED)	50 Ω
Temperature (LED)	290 K
Noise figure (LED)	8 dB
Dark current (LED)	50 nA
Background current (LED)	20 μA

Table 2.2: Parameters used in the numerical experiments.

By simple geometry considerations and adopting the models of Section 2.3, we calculated the optical power at the input of the receiver (tag or LED)

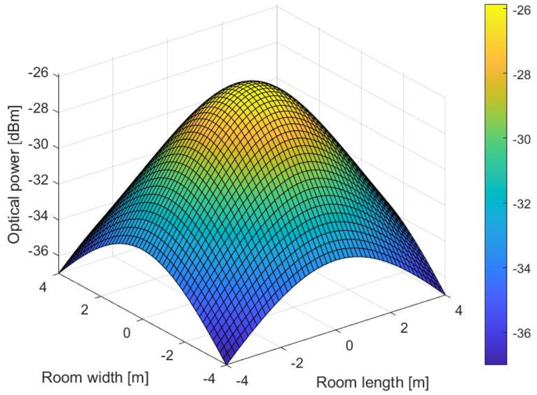

Figure 2.2: Optical RX power in DL for a tag moved around the room.

by moving the tag across the room, which is discretized as a square grid with a spacing of 16 cm in both width and length.

In Figs. 2.2 and 2.3, we reported the received power (in dBm) as a function of the tag position for both DL and UL, respectively, using equations (2.7) for DL and (2.12) for UL. As expected, due to the passive backscatter mechanism in UL, the values of the received power are much lower in UL compared to DL.

In Fig. 2.4, the theoretical BER distribution in the room caused by the UL LOS channel is shown, based on (2.38). As expected, at the center of the ceiling the values of BER are extremely good, since the optical power received by the LED takes on its maximum value. On the other hand, the BER results are less satisfactory in the room corners. However, it is noteworthy that the gradient of the BER surface assumes very small values inside the square of size 4 m $\times$ 4 m centered at the origin, which means that the BER does not vary significantly in this spatial region, as shown in Figs. 2.5 and 2.6.

In Fig. 2.7, the values of BER are plotted as a function of the LED half power angle, which is varied from 30° to 60° with steps of 5°, for a fixed tag position at the center of the room. Results show that with the increase of LED half power angle, the BER also increases. The reason behind this behav-

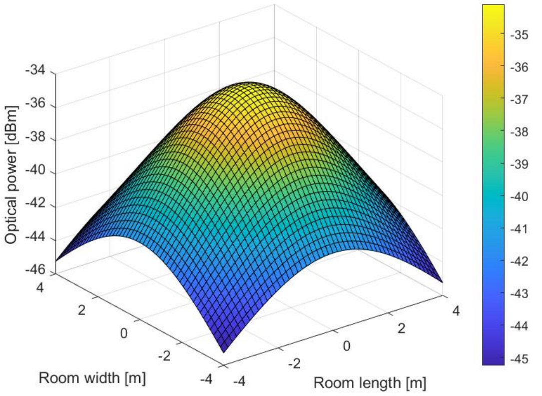

Figure 2.3: Optical RX power in UL for a tag moved around the room.

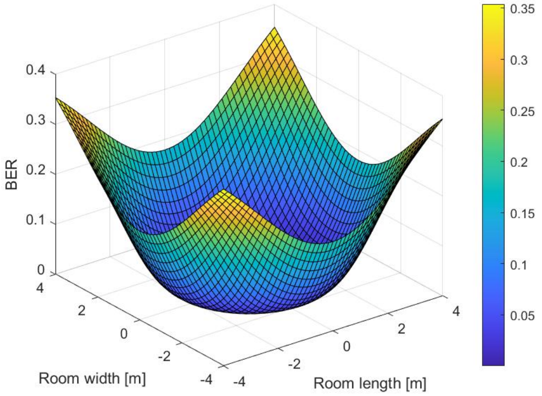

Figure 2.4: BER in UL for a tag moved around the room.

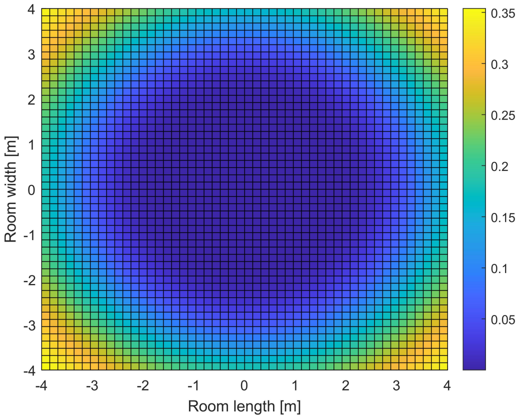

Figure 2.5: 2D view of BER in UL for a tag moved around the room.

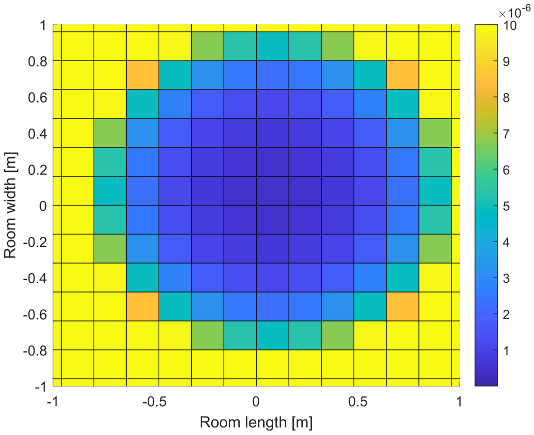

Figure 2.6: Zoomed view in the center of room of BER of Fig. 2.5.

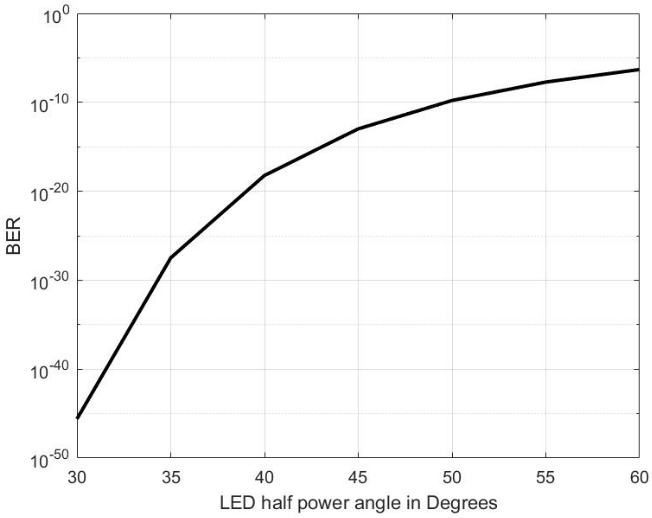

Figure 2.7: BER in UL as a function of LED half power angle.

ior is that, with the increase in angle, the light beam becomes wider and less focused, which causes less reflected power and consequently, a performance degradation of the bit decision process.

Finally, Fig. 2.8 shows the relation between BER and the LED power, which is increased from 0.1 Watt to 1 Watt in steps of 0.1 W. The corresponding BER curve monotonically decreases as the LED power increases. Specifically, it is seen that very satisfactory BER values can be obtained with small LED powers. For instance, a BER of 10^{-6} is attained with a LED power as little as 0.8 W.

2.7 Conclusions

We provided physics-based models for DL and UL of a VLBC systems for e-Health applications. A theoretical end-to-end performance analysis in terms of BER was also carried out, which takes into account the main sources of noise and physical parameters of the system. The proposed models and theoretical formulas can be used to accurately predict the performance of a VLBC system

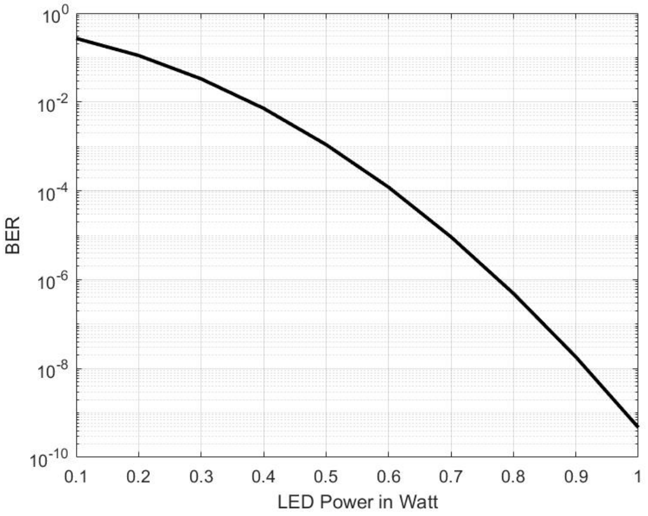

Figure 2.8: BER in UL as a function of LED power.

working particularly in indoor hospital environments.

Chapter 3

VLB channel estimation and equalization

In this Chapter[1], in order to improve the accuracy of the model proposed in Chapter 2 and assess the system performance in a more realistic setting, we have added channel estimation and equalization in VLB system modelling. To this aim, in this Chapter we first introduce the UL packet structure, then we derive the discrete-time model that allows one to perform channel estimation and equalization at the RX side. Finally, we report the results of Monte Carlo simulations, aimed at assessing the BER[2] performance of the overall VLBC system.

3.1 UL packet structure

In the following, we assume that UL transmission at the tag is organized in *packets*, each one comprising a *preamble* of B_t training symbols followed by

---

[1] The content of this Chapter is mainly based on Reference 4 of the Author's publication list.

[2] Although we deal with packet-based transmission in this Chapter, we still chose to use BER as a performance metric instead of packet error rate (PER), as BER provides a more fine-grained measure of the quality of the transmission at the bit level. Moreover, a meaningful evaluation of PER should necesseraly include the effects of channel coding, which we did not consider in our simulations.

a *payload* of B_d data symbols, for a total of $B_{\text{ul}} \triangleq B_t + B_d$ symbols. The structure of the packet is depicted in Fig. 3.1, where, for more generality, a guard time T_g is interposed between the preamble and data sections, whose length is sufficient to accommodate the dispersion of the overall channel. The packet structure is designed to accommodate different formats of healthcare data.

3.2 Receiver processing

The received signal at the LED is given by (2.27), which is repeated here for convenience:

$$\begin{aligned} r(t) &= \beta_{\text{ul}}\, s_{\text{ul}}(t-\tau_{\text{ul}}) * h_{\text{rx}}(t) + w(t) \\ &= \sum_{\ell=-\infty}^{\infty} u[\ell]\, h_{\text{ul}}(t-\tau_{\text{ul}}-\ell\, T_{\text{ul}}) + w(t) \end{aligned} \tag{3.1}$$

where $s_{\text{ul}}(t)$ is the signal to be transmitted by the tag in UL, $h_{\text{rx}}(t)$ is the impulse response of the RX filter, and $h_{\text{ul}}(t) = \beta_{\text{ul}}\, p_{\text{ul}}(t) * h_{\text{rx}}(t)$ is the impulse response of the overall channel.

In the following, we assume that the RX has acquired symbol synchronization, i.e., it knows the value of τ_{ul}: since the scenario is static, this information can be obtained quite easily, with standard techniques. Without restrictions, we set $\tau_{\text{ul}} = 0$ in (2.27) to simplify the following derivations, yielding:

$$r(t) = \sum_{\ell=-\infty}^{\infty} u[\ell]\, h_{\text{ul}}(t-\ell\, T_{\text{ul}}) + w(t) \tag{3.2}$$

The receiver has to perform two tasks:

1. it performs *channel estimation*, based on the B_t known training symbols of the preamble;
2. equipped with knowledge of the channel, it *equalizes* the channel to estimate the B_d data symbols of the payload.

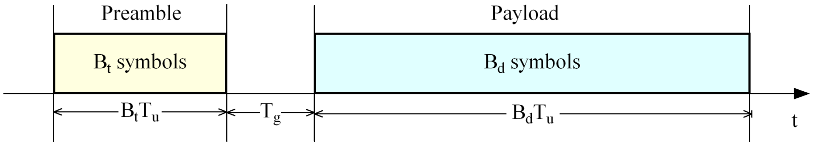

Figure 3.1: UL packet structure.

Note that, even if LOS propagation is assumed, channel estimation is still needed, since we must compensate for the non-ideal response of the LCD shutter and for any unknown degradation introduced in the TX-RX chain. Our channel estimation procedure allows the VLB system to work satisfactorily without requiring cumbersome calibration procedures, and allowing the system to easily adapt to the unknown characteristics of the devices.

For performing channel estimation and equalization, it is convenient to resort at the RX to *symbol-based sampling*, i.e., the received signal is sampled, after RX filtering, with rate $1/T_{\text{ul}}$.

Channel estimation

For channel estimation, the receiver samples the signal $r(t)$ given by (3.2) at times $t_n = n\,T_{\text{ul}} + \tau_0$ in the interval $(0, B_t\,T_{\text{ul}})$, obtaining thus B_t symbol-spaced samples:

$$r[n] = \sum_{\ell=0}^{B_t-1} u[\ell]\,h_{\text{ul}}[n-\ell] + w[n]\,, \qquad n = 0, 1, \ldots, B_t - 1 \tag{3.3}$$

where $r[n] \triangleq r(t_n)$, $h_{\text{ul}}[n] \triangleq h_{\text{ul}}(t_n)$, and $w[n] \triangleq w(t_n)$. The value of τ_0 (sampling delay) should be chosen so as to maximize $h_{\text{ul}}(t_n)$, that is, to open the eye diagram [91].

By stacking the obtained samples in the column vector $\boldsymbol{r}_t = [r[0], r[1], \ldots, r[B_t - 1]]^{\text{T}} \in \mathbb{R}^{B_t}$, we get:

$$\boldsymbol{r}_t = \boldsymbol{U}_t\,\boldsymbol{h}_{\text{ul}} + \boldsymbol{w} \tag{3.4}$$

where (see [101, Example 4.3]) $\boldsymbol{U}_t \in \mathbb{R}^{B_t \times B_t}$ is the Toeplitz matrix of the training symbols, whose first column and row are $[u[0], u[1], \ldots, u[B_t - 1]]^{\mathrm{T}}$ and $[u[0], 0, 0, \ldots, 0]$, respectively, whereas $\boldsymbol{h}_{\text{ul}} = [h_{\text{ul}}[0], h_{\text{ul}}[1], \ldots, h_{\text{ul}}[B_t - 1]]^{\mathrm{T}} \in \mathbb{R}^{B_t}$ contains the channel samples to be estimated, and $\boldsymbol{w} = [w[0], w[1], \ldots, w[B_t - 1]]^{\mathrm{T}} \in \mathbb{R}^{B_t}$ is the noise vector, whose elements are T_{ul}-spaced samples of $w(t)$.

We assume that the elements of vector $\boldsymbol{w}$ are statistically independent and can be approximated as Gaussian, with a finite but unknown variance $\sigma_w^2 = \sigma_{\text{therm}}^2 + \sigma_{\text{shot}}^2$. Moreover, since we assume that the ambient shot noise is predominant, we neglect here any variation of σ_{shot}^2 with the transmitted training symbol. Thus, the variance σ_w^2 can be evaluated as

$$\sigma_w^2 = \frac{N_0}{2} \int_{-\infty}^{+\infty} |H_{\text{rx}}(f)|^2 \, df = \frac{N_0}{2} \int_{-\infty}^{+\infty} |h_{\text{rx}}(t)|^2 \, dt \tag{3.5}$$

where $H_{\text{rx}}(f)$ is the Fourier transform of $h_{\text{rx}}(t)$, and N_0 is given by (2.31).

Since vector $\boldsymbol{w}$ has a diagonal covariance matrix, the maximum-likelihood (ML) estimate of the channel can be obtained straightforwardly by solving the following problem:

$$\min_{\boldsymbol{h}_{\text{ul}}} \|\boldsymbol{r}_t - \boldsymbol{U}_t \, \boldsymbol{h}_{\text{ul}}\|^2 \tag{3.6}$$

whose solution [101, Theorem 4.1] is also referred to as the *minimum variance unbiased* (MVU) estimator:

$$\hat{\boldsymbol{h}}_{\text{ul}} = (\boldsymbol{U}_t^{\mathrm{T}} \boldsymbol{U}_t)^{-1} \boldsymbol{U}_t^{\mathrm{T}} \, \boldsymbol{r}_t \tag{3.7}$$

This estimator is efficient in the sense that it attains the CRLB bound [101] under mild conditions.

Equalization and data detection

For equalization and data detection, the receiver samples the received signal $r(t)$ given by (3.2) at times $t_n = B_t T_{\text{ul}} + T_g + n T_c$ in the interval $(B_t T_{\text{ul}} +$

$T_g, B_t T_{\text{ul}} + T_g + B_d T_{\text{ul}})$, obtaining thus

$$r[n] = \sum_{\ell=0}^{B_d-1} u[\ell]\, h_{\text{ul}}[n-\ell] + w[n]\,, \qquad n = 0, 1, \ldots, B_d - 1 \tag{3.8}$$

where $r[n] \overset{\triangle}{=} r(t_n)$, $h_{\text{ul}}[n] \overset{\triangle}{=} p(t_n)$, and $w[n] \overset{\triangle}{=} w(t_n)$.

By stacking the B_d consecutive symbol-spaced samples $r[n]$ in the column vector $\boldsymbol{r}_d = [r[0], r[1], \ldots, r[B_d - 1]]^{\text{T}} \in \mathbb{R}^{B_d}$, we get

$$\boldsymbol{r}_d = \boldsymbol{H}_{\text{ul}}\, \boldsymbol{u}_d + \boldsymbol{w} \tag{3.9}$$

where $\boldsymbol{H}_{\text{ul}} \in \mathbb{R}^{B_d \times B_d}$ is the Toeplitz matrix of the channel, whose first column and row are $[h_{\text{ul}}[0], h_{tu}[1], \ldots, h_{\text{ul}}[B_d - 1]]^{\text{T}}$ and $[h_{\text{ul}}[0], 0, 0, \ldots, 0]$, respectively, whereas $\boldsymbol{u}_d = [u[0], u[1], \ldots, u[B_d - 1]]^{\text{T}} \in \mathbb{R}^{B_d}$ contains the data symbols to be estimated, and $\boldsymbol{w} = [w[0], w[1], \ldots, w[B_d - 1]] \in \mathbb{R}^{B_d}$ is the noise vector, whose elements are T_{ul}-spaced samples of $w(t)$.

Assuming at first that $\boldsymbol{H}_{\text{ul}}$ is known, since vector $\boldsymbol{w}$ has a diagonal covariance matrix, the maximum-likelihood (ML) estimate of the symbols can be obtained straightforwardly by solving the following problem:

$$\min_{\boldsymbol{u}_d} \|\boldsymbol{r}_d - \boldsymbol{H}_{\text{ul}}\, \boldsymbol{u}_d\|^2 \tag{3.10}$$

whose solution is again the MVU estimator:

$$\hat{\boldsymbol{u}}_d = (\boldsymbol{H}_{\text{ul}}^{\text{T}} \boldsymbol{H}_{\text{ul}})^{-1} \boldsymbol{H}_{\text{ul}}^{\text{T}}\, \boldsymbol{r}_d \tag{3.11}$$

This estimator is efficient in the sense that it attains the CRLB bound [101] under mild conditions. By replacing $\boldsymbol{H}_{\text{ul}}$ with $\hat{\boldsymbol{H}}_{\text{ul}}$, built from the previously obtained channel estimates given by (3.7), we obtain the *soft* symbol estimates as

$$\hat{\boldsymbol{u}}_d = (\hat{\boldsymbol{H}}_{\text{ul}}^{T} \hat{\boldsymbol{H}}_{\text{ul}})^{-1} \hat{\boldsymbol{H}}_{\text{ul}}^{T} \boldsymbol{r}_d \tag{3.12}$$

where $\hat{\boldsymbol{H}}_{\text{ul}}$, built from the previously obtained channel estimates, is used *in* *lieu* of the true $\boldsymbol{H}_{\mathrm{ul}}$. The final *hard* symbol estimates are obtained by comparing the elements of $\hat{\boldsymbol{u}}_d$ with a suitably chosen threshold, i.e., by performing a quantization of the elements of $\hat{\boldsymbol{u}}_d$

3.3 Simulation results

Since a theoretical BER performance analysis, although not impossible in principle, is complicated by the channel estimation step, we present in this Section the results of Monte Carlo computer simulations, carried out over 10^6 iterations. A large room with dimensions 8 m $\times$ 8 m $\times$ 4 m is considered, which is a scenario similar to that of Chapter 2. The detail of simulations parameters is given in Tab. 3.1.

Parameters	**Values**
Room dimensions	8 m $\times$ 8 m $\times$ 4 m
Modulation scheme	OOK
Bit-interval	3 ms, 6 ms, 8 ms
LED location	Center of the ceiling
Tag location	At position $(5, 5, 0)$ (on the floor)
RR efficiency (tag)	0.60
TX power (LED)	10^{-5}–10^{-2} W
TX semi-angle (LED)	60°
FOV of concentrator (LED)	90°
PD area (LED)	30 mm^2
PD responsivity (LED)	0.4 A/W
OF gain (LED RX)	0.5
Load resistor (LED)	50 Ω
Temperature (LED)	290 K
Noise figure (LED)	10 dB
Dark current (LED)	50 nA
Background current (LED)	20 μA
Number of training symbols/packet	4
Number of data symbols/packet	30

Table 3.1: Parameters used in the Monte Carlo simulations.

The discrete-time model is first generated in Matlab by assuming to sample its continuous-time counterpart at rate P/T_{ul}, that is, we apply a rather high oversampling factor ($P = 8$) in all the simulations, which allowed us to plot in Matlab the signals along the communication chain as continuous-time waveforms. Where appropriate, the rate is suitably reduced to 1 sample/symbol by simple decimation.

In order to simulate the LCD shutter response, and keeping in view the disparity between charging time and discharging time of the LCD shutter, realistic charging constant and discharging time constant parameters are used [26]. The adopted LCD shutter waveform is modeled by the following expression:

$$p_{\text{ul}}(t) = \begin{cases} 1 - \exp(-t/\tau_c)\,, & 0 \le t \le T_1\,; \\ \alpha\ \exp(-(t - T_1)/\tau_d)\,, & T_1 \le t \le T_2\,; \\ 0\,, & \text{elsewhere}\,; \end{cases} \tag{3.13}$$

where $\alpha = 1 - \exp(-T_1/\tau_c)$, $T_1 = T_{\text{ul}}$, $T_2 = T_{\text{ul}} + 5\tau_d$, with τ_c and τ_d representing the charge/discharge time constants, respectively. The oversampled version of the LCD shutter waveform modeled by (3.13) is shown in Fig. 3.2 for $T_u = 8$ ms, $\tau_c = 1$ ms, and $\tau_d = 4$ ms.

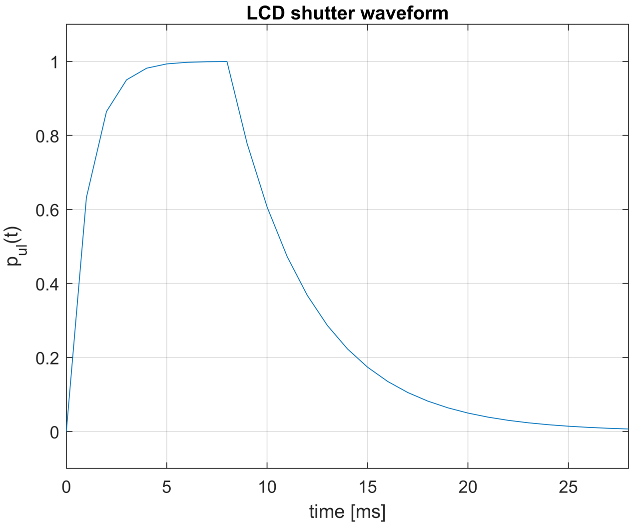

Figure 3.2: LCD shutter response waveform for $T_u = 8$ ms, $\tau_c = 1$ ms, and $\tau_d = 4$ ms.

A plot of the oversampled versions of the transmitted and received signal for $T_u = 8$ ms is given in Fig. 3.3, where $s_{\text{ul}}(t)$ is the backscatter optical signal given by (2.17), $i(t)$ is the ideal (noise-free) current signal received after PD [see (2.25)], and $r(t)$ is the current noisy signal after RX filtering (before sampling and equalization), i.e., it corresponds to (2.26). In our simulations, we assume that RX filtering is performed by means of a simple *integrate-and-dump* filter, i.e., $h_{\text{rx}}(t)$ has a rectangular shape.

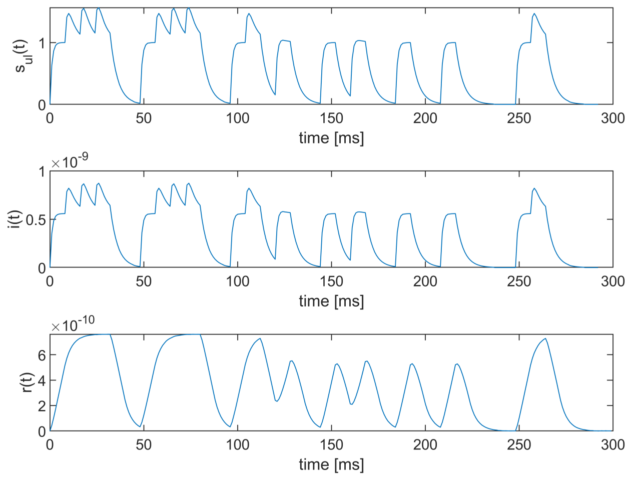

Figure 3.3: Transmitted and received signals: $s_{\text{ul}}(t)$ is the backscatter TX signal given by (2.17) (upper), $i(t)$ is the noise-free current RX signal given by (2.25) (middle), $r(t)$ is the current noisy signal after RX filtering given by (2.26) (lower).

Preliminarily, to assess the effectiveness of channel estimation, in Fig. 3.4 we show the oversampled discrete-time versions of the overall channel $h_{\text{ul}}(t)$ given by (2.28) (upper plot), together with its symbol-spaced version (middle plot), and the result of the channel estimation procedure (lower plot), for $T_{\text{ul}} = 8$ ms. These curves show that the channel estimation procedure is able to accurately estimate the channel.

In Fig. 3.5, the graph of BER versus the transmitted LED power is shown. The simulations are repeated for three values of the symbol interval $T_{\text{ul}} \in (3, 6, 8)$ ms, which correspond to the data-rates $R_b \in (1/3, 1/6, 1/8)$ kb/s. Moreover, a comparison between two RXs employing or not the channel estimation/equalization procedure is presented, which shows that with the

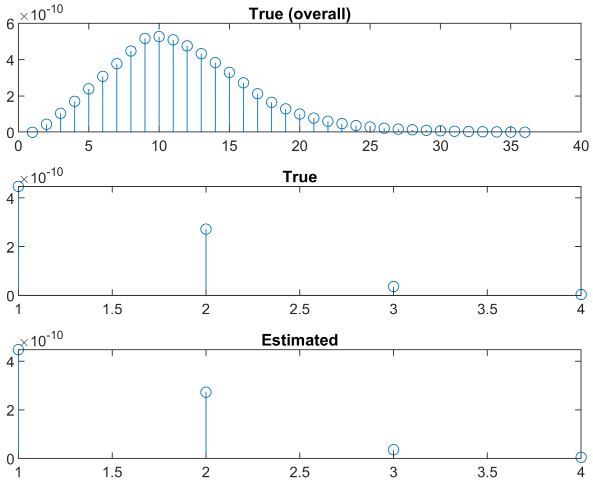

Figure 3.4: Channel estimation: oversampled overall channel (upper), symbol-spaced overall channel (middle), estimated channel (lower).

use of channel equalization a better BER performance is achieved, especially when the bit-rate increases and, hence, the effects of ISI are more relevant. In particular, it can be observed that for the RX not employing equalization, a BER floor is obtained with increasing LED power values (the floor is indeed very high for $T_{\mathrm{ul}} = 3$ ms, which makes the system completely out-of-service in this case). Moreover, it has been observed that, as expected, a better system performance is achieved when the data-rate is decreased. For some ranges of LED power, variable with T_{ul}, the need to resort to equalization could be overcome, but equalization is needed whenever the system is required to attain very small BER values.

In Fig. 3.6, a plot of the BER as a function to LED half power angle is shown, for $T_{\mathrm{ul}} = 3$ ms and LED power equal to 3 mW. A comparison between equalized and non equalized channel is presented, which shows with the use of channel equalization, better system performance, with respect to BER, is achieved. Moreover, it has been observed that with the decrease in the half

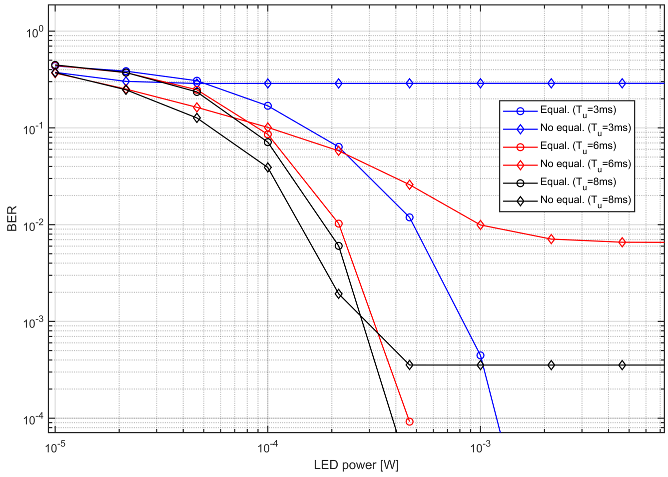

Figure 3.5: BER in UL as a function of LED power, for different values of the bit interval T_{ul}, for a RX employing equalization and a RX without equalization.

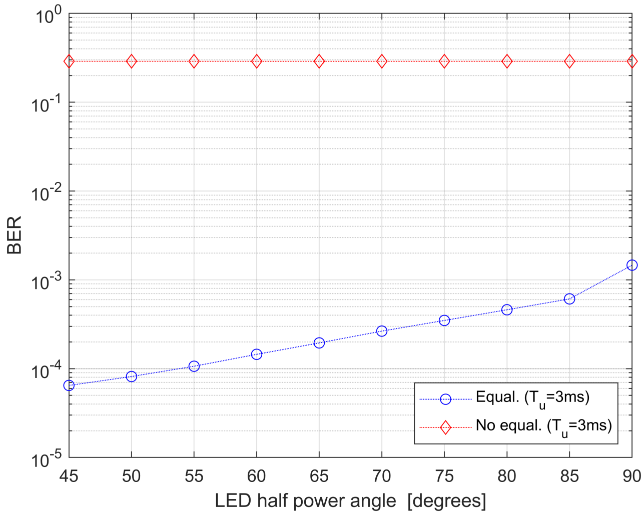

Figure 3.6: BER in UL as a function of LED half power angle, for $T_{\mathrm{ul}} = 3$ ms and fixed LED transmitted power equal to 3 mW.

power angle, better values of BER are achieved. The less half power angle, the more concentrated optical power will be and consequently, lower BER values are achieved.

3.4 Conclusion

The end-to-end performance analysis of a VLBC system, in terms of BER, has been carried out, with the help of Monte Carlo simulations. Different from the model in Chapter 2, the analysis in this Chapter includes the effects of the LCD shutter response, with realistic charging/discharging time constant parameters, Particularly, the impact of employing a training-based channel estimation/equalization procedure at the RX is investigated. It is observed that, with the use of channel equalization, a better BER performance is achieved, especially when the data-rate is higher. In particular, adoption of equalization allows one to avoid the annoying BER floor phenomenon.

Chapter 4

Future research directions

Although VLB is a promising paradigm for IoT, there are some inherent issues to be dispelled, which deserve further developments in order to ensure a widespread use of such a novel technology. In this Chapter, we delineate the most interesting future research directions.[1]

4.1 Channel modeling for VLB applications

As already pointed out in Section 2.3, many works dealing with channel modeling of optical wireless communications are targeted at the IR region of electromagnetic spectrum. However, there exist significant differences between VLB and IR communications and those results cannot be applied to VLB channel modeling in a straightforward manner. For instance, an IR source can be approximated as a monochromatic emitter, while a visible light LED source is inherently wideband. This fact implies that wavelength-dependency of the source in VLB channel modeling should be accounted for. Moreover, in IR communications, the reflectance of materials is typically modeled as a constant. In contrast, the reflectance of materials in the VLB spectrum should be taken into consideration due to the wideband nature of VLB links, especially

---

[1] The content of this Chapter is mainly based on References 1 and 3 of the Author's publication list.

for the reflection process at the tag.

As a matter of fact, a precise characterization of the VLB channel is needed, by also considering the case of multiple sources and/or hybrid PD-based and camera-based tags [102]. Specifically, advantages and drawbacks of the VLB medium have to be compared to those of IR media. Physical characteristics of VLB channels using IM/DD are not fully studied, including path losses and multipath responses. Another key issue is the characterization of natural and artificial ambient VLB noise.

4.2 VLBC system throughput

A technology can be regarded as "mature" if its performance characteristics are well-understood with well-established design specifications. In this respect, the *throughput* is a measure of the long-term average rate of a VLBC system, which represents a key performance metric for system designs. The indoor point-to-point VLC system throughput has been studied in [103, 104]. Extension of such works to the VLBC case is not straightforward, due to further constraints regarding spatial location and system geometry. The results of [105] work well for OOK/PAM modulation and can be applied to VLBC systems. System throughput of optical channels with IM/DD is more complicated due to some additional constraints that differ from the conventional electrical or radio systems [106, 107, 108]. Specifically, in IM/DD optical systems, the information is modulated as the instantaneous optical intensity and, therefore, this peculiarity places three constraints on the transmitted signal.

The first constraint arises from the fact that the transmitted signal must be non-negative. Moreover, the eye safety requirements limit the transmit power that may be used. Eye safety limitations are generally expressed in terms of exposure duration at a specific optical power [109], which translates to a second *average* constraint on the optical power [110]. A third *peak* constraint also arises due to safety requirements [111] and, additionally, in order to avoid saturation of the optical power (or the device burns). Evaluation of the system throughput under such three constraints is challenging even for conventional

Tuning element	**Tuning mechanism**	**Operation spectrum**	**Max modulation speed**
Transparent conductive oxides	Electrical	VL	10 MHz
Ferroelectrics	Electrical/Thermal/Optical	GHz to VL	NA
Graphene	Electrical	THz to VL	20 GHz
Phase change materials	Optical	THz to VL	2.77 GHz
Liquid crystals	Electrical/Thermal/Optical	GHz to VL	1 kHz
Semiconductors	Electrical/Optical	THz to VL	1.2 GHz
Elastic materials	Mechanical	GHz to VL	NA
M-NEMS	Electrical	GHz to VL	1.5 kHz

M-NEMS = Micro-NanoElectroMechanical Systems

Table 4.1: Different types of metasurfaces suitable for VLB applications.

VLC applications, for which closed-form expressions are still unknown [110].

In the case of VLBC applications, calculation of the system throughput is even more complicated due to the additional fact that the UL channel is *double Gaussian* (i.e., it is the product of two Gaussian random variables) due to the reflection process performed by the tag. Therefore, throughput bounds and asymptotics are essential to understand the ultimate performance limits of VLBC systems.

4.3 Metasurface-based VLB

The degree of directionality of the source and the tag significantly impacts on the VLB system performance, especially when the signal transmitted by the source is concentrated in a very narrow beam and/or the tag is characterized by a narrow field-of-view (FoV). Standard mirrors, such as optical RRs, can support only specular reflections (i.e., the incident angle and the reflection angle are identical). Consequently, mechanical change of their orientation is needed in order to reflect the beam in a desired direction.

An interesting alternative is represented by the use of gradient *metasurfaces* [112], which are synthetic materials composed of sub-wavelength metallic or dielectric structures capable of steering the incident illumination toward directions not predicted by Snell's law [113, 114, 115]. In optics, they have been used as *reconfigurable intelligent surfaces* (RISs) for the realization of artificial multichannel communication systems, aimed at improving system performance [51] or for energy efficiency maximization in VLC systems [116]. Moreover, a metasurface can also be used as a RR, albeit with much higher efficiency [117, 118], or as a VLC modulator [119, 120]. Tuning mechanisms of RISs for VLB applications are summarized in Table 4.1, along with their main characteristics.

Apart from their physical implementation, metasurfaces can be used in VLB systems in different arrangements. They can replace the RR and/or LCD shutter modulator, assuring higher efficiency, focusing capabilities, improved speed and flexibility in implementing more sophisticated modulation/coding schemes. Another usage is to improve *TX/RX efficiency*, possibly solving obstruction problems in LOS links between the source and the tag. However, there are several issues that can hinder the applicability of metasurfaces to VLB systems. First, the mathematical modeling of metasurfaces is generally involved (based on the solution of integral equations), and simple signal models, useful for system-level design, are lacking. Second, switching frequencies of current metasurfaces are inadequate for IoT applications and faster switching mechanisms based on innovative phase transition materials have to be exploited. Third, existing studies rely on space-domain design techniques only, i.e., the phase profile of the metasurface is intentionally varied by changing the state of its sub-wavelength elements at different spatial positions on the metasurface. It would be interesting to also exploit the temporal dimension of the metasurface, by varying in time the phase response of its sub-wavelength elements [121].

Space-time metasurfaces may be used to also realize out-of-band full-duplex VLB systems, for which auto-interference can be readily counteracted. Indeed, they allow to control both spatial (propagation direction) and spectral (frequency distribution) characteristics of the scattered light, thus allowing to separate at the UL RX the signal emitted by the source and the signal backscattered by the tag in the frequency domain [122].

4.4 Multiple access schemes for massive VLB-enabled IoT

Massive IoT refers to applications that are less latency sensitive and have relatively low throughput requirements, but demand a huge volume of low-cost, low-energy consumption devices on a network with excellent coverage. The problem of designing multiple access schemes that are able to deal with the limited capabilities of the tags is still an open issue for conventional VLC [123] and it has only recently attracted attention [124, 125, 126, 127].

In the literature of VLBC, very few works consider the problems of supporting multiple tag communications. A notable exception is RetroI2V [45], where *ad hoc* signaling protocols have been developed to detect and resolve collisions in DL/UL of an infrastructure-to-vehicle communication and networking system. Another interesting contribution is RetroMUMIMO [49], which combines MIMO-like decoding with contention-based MAC to support low-latency concurrent tag transmissions.

In our opinion, *non-orthogonal multiple-access* (NOMA) schemes [128] are more suitable for VLBC in massive IoT applications than their orthogonal counterparts, since the latter ones may require an unsustainable signaling overhead. NOMA techniques can broadly be divided into two categories, namely, *power-domain* and *code-domain* ones, wherein multiplexing is achieved by transmitting with different powers or different codes, respectively.

A power-domain NOMA scheme for conventional VLC has been proposed in [129], which implements successive interference cancellation to remove interference effects. The benefits of power-domain NOMA for VLBC have not been studied yet. On the other hand, code-domain NOMA schemes exhibit an inherent robustness against ambient reflections, i.e., the interference deriving from light reflected by other objects (such as walls or furnitures) in the ambient, by allowing easy separation of the desired signal from reflections at the RX. However, code-domain NOMA could be difficult to implement with LCD shutter modulators, due to their limitations in switch speed [31]. Use of alternative faster modulators, like RR-based or metasurface-based ones, would allow one to use code-domain NOMA schemes, improving thus system performance.

Conclusions

VLB is a new research field, where a number of interesting solutions have been proposed and prototyped, but many challenges and open problems still exist, both theoretical and practical ones. In particular, VLB is useful whenever a strong illumination infrastructure is available and in environments where the lights are always switched on, such as many healthcare facilities. Moreover, VLB techniques can also be profitably used outdoors, due to the availability of a natural source like the sun, which can assure high illumination levels for a significant fraction of time. Shortly, VLB techniques are among the most "biologically friendly" and "green" techniques.

Similar to any wireless communication system, the propagation channel as well as the characteristics of source/tag front-ends dictate the fundamental limits on the physical layer performance of VLB system. Realistic propagation channel models are therefore of utmost importance for VLB system design, performance evaluation, and testing.

In this thesis, we considered the characteristics and physical-layer treats regarding VLB, with a focus on IoT indoor applications. Thus, the main findings of this thesis regards VLB link characterization and performance analysis, together with analysis of some problems typical of digital wireless communications, such as channel estimation and equalization. Particularly, we have dealt with several theoretical issues, regarding link modeling, signal and noise characterization, performance analysis, channel estimation and equalization. We have considered some fundamental theoretical issues and derived simple yet accurate mathematical models, which are further validated by computer simulation results.

As future resarch directions, a particularly interesting field is the adoption of metasurfaces in VLB, which could definitely replace simple RRs and LCD shutters by allowing increased flexibility and adaptivity. Finally, the design of multiple access schemes for VLB channels might facilitate the realization of the massive IoT vision, according to which a massive number of low-cost and low-energy sensors, devices, objects, and machines might communicate with each other.

Author's publications

Publications inherent to the thesis

1. M.H. Ullah, G. Gelli, and F. Verde, "Visible light backscattering with applications to communication and localization in healthcare: A survey,", in *Procedia Computer Science*, vol. 203, pp. 745–752, August 2022.
2. M. H. Ullah, G. Gelli, and F. Verde, "Visible light backscattering communications in healthcare scenarios: link modeling and performance analysis," in *Proc. of 2022 IEEE International Conference on Internet of Things and Intelligence Systems* (IoTaIS), Bali, Indonesia, pp. 179–185, November 2022 (won 2nd Best Paper Award).
3. M. H. Ullah, G. Gelli, and F. Verde, "Visible light backscattering with applications to the Internet of Things: State-of-the-art, challenges, and opportunities," Under-review for publication in *Internet of Things*, 2023.
4. M. H. Ullah, G. Gelli, and F. Verde "Visible light backscattering communications: link modeling and performance analysis with channel Equalization and channel estimation," to be submitted to *IEEE Journal on Lightwave Technologies*, 2023.

Other publications

5. A. Umair, E. Masciari, M.H. Ullah, "Sentimental analysis applications and approaches during COVID-19: a survey," In *Proc. of 25th Interna-*

tional Database Engineering & Applications Symposium (IDEAS'21), Montreal, Canada, pp. 304–308, July 2021.

6. A. Umair, M.S. Sarfraz, M. Ahmad, U. Habib, M.H. Ullah, and M. Mazzara, "Spatiotemporal analysis of web news archives for crime prediction," *Applied Sciences*, vol. 10, no. 22, p. 8220, November 2020.
7. A. Umair, E. Masciari, G. Madeo, and M.H. Ullah, "Applications of Majority Judgement for Winner Selection in Eurovision Song Contest," in *Proc. of the 26th International Database Engineered Applications Symposium (IDEAS'22)*, Budapest, Hungary, pp. 113–119, August 2022.
8. A. Umair, E. Masciari, G. Madeo, and M.H. Ullah, "Sentimental Analysis of COVID-19 Vaccine Tweets using BERT+NBSVM, in *Proc. of New Frontiers in Mining Complex Patterns (NFMCP'22)*, Grenoble, France, September 2022.

Bibliography

[1] P. H. Pathak, X. Feng, P. Hu, and P. Mohapatra, “Visible light communication, networking, and sensing: A survey, potential and challenges,” *IEEE Communications Surveys and Tutorials*, vol. 17, no. 4, pp. 2047–2077, 2015.

[2] J. Luo, L. Fan, and H. Li, “Indoor positioning systems based on visible light communication: State of the art,” *IEEE Communications Surveys and Tutorials*, vol. 19, no. 4, pp. 2871–2893, 2017.

[3] Y. Zhuang, L. Hua, L. Qi, J. Yang, P. Cao, Y. Cao, Y. Wu, J. Thompson, and H. Haas, “A survey of positioning systems using visible LED lights,” *IEEE Communications Surveys & Tutorials*, vol. 20, no. 3, pp. 1963–1988, 2018.

[4] M. F. Keskin, A. D. Sezer, and S. Gezici, “Localization via visible light systems,” *Proceedings of the IEEE*, vol. 106, no. 6, pp. 1063–1088, 2018.

[5] S. Ma, Q. Liu, and P. C.-Y. Sheu, “Foglight: Visible light-enabled indoor localization system for low-power IoT devices,” *IEEE Internet of Things Journal*, vol. 5, no. 1, pp. 175–185, 2018.

[6] X. Liu, X. Wei, and L. Guo, “DIMLOC: Enabling high-precision visible light localization under dimmable LEDs in smart buildings,” *IEEE Internet of Things Journal*, vol. 6, no. 2, pp. 3912–3924, 2019.

[7] F. Alam, N. Faulkner, and B. Parr, “Device-free localization: A review of non-RF techniques for unobtrusive indoor positioning,” *IEEE Internet of Things Journal*, vol. 8, no. 6, pp. 4228–4249, 2021.

[8] K. Majeed and S. Hranilovic, “Passive indoor visible light positioning system using deep learning,” *IEEE Internet of Things Journal*, vol. 8, no. 19, pp. 14810–14821, 2021.

[9] X. Liu, X. Wei, L. Guo, and S. Song, “DarkVLP: “lights-off" visible-light positioning,” *IEEE Internet of Things Journal*, vol. 9, no. 13, pp. 11071–11084, 2022.

[10] D. Karunatilaka, F. Zafar, V. Kalavally, and R. Parthiban, “LED based indoor visible light communications: State of the art,” *IEEE Communications Surveys and Tutorials*, vol. 17, no. 3, pp. 1649–1678, 2015.

[11] R. Want, “An introduction to RFID technology,” *IEEE Pervasive Computing*, vol. 5, no. 1, pp. 25–33, 2006.

[12] V. Liu, A. Parks, V. Talla, S. Gollakota, D. Wetherall, and J. R. Smith, “Ambient backscatter: Wireless communication out of thin air,” *SIGCOMM Comput. Commun. Rev.*, vol. 43, pp. 39—-50, Aug. 2013.

[13] A. N. Parks, A. Liu, S. Gollakota, and J. R. Smith, “Turbocharging ambient backscatter communication,” *SIGCOMM Comput. Commun. Rev.*, vol. 44, pp. 619—630, Aug. 2014.

[14] D. Darsena, G. Gelli, and F. Verde, “Modeling and performance analysis of wireless networks with ambient backscatter devices,” *IEEE Transactions on Communications*, vol. 65, no. 4, pp. 1797–1814, 2017.

[15] D. Darsena, G. Gelli, and F. Verde, “Cloud-aided cognitive ambient backscatter wireless sensor networks,” *IEEE Access*, vol. 7, pp. 57399–57414, 2019.

[16] A. Aljaberi, P. C. Sofotasios, and S. Muhaidat, “Modulation schemes for visible light communications,” in *2019 International Conference on*

Advanced Communication Technologies and Networking (CommNet), pp. 1–10, 2019.

[17] H. Wymeersch, J. Lien, and M. Z. Win, "Cooperative localization in wireless networks," *Proceedings of the IEEE*, vol. 97, no. 2, pp. 427–450, 2009.

[18] R. M. Buehrer, H. Wymeersch, and R. M. Vaghefi, "Collaborative sensor network localization: Algorithms and practical issues," *Proceedings of the IEEE*, vol. 106, no. 6, pp. 1089–1114, 2018.

[19] L. Zhou, J. M. Kahn, and K. S. J. Pister, "Corner-cube retroreflectors based on structure-assisted assembly for free-space optical communication," *Journal of Microelectromechanical Systems*, vol. 12, no. 3, pp. 233–242, 2003.

[20] S. Junique, D. Agren, Q. Wang, S. Almqvist, B. Noharet, and J. Y. Andersson, "A modulating retro-reflector for free-space optical communication," *IEEE Photonics Technology Letters*, vol. 18, no. 1, pp. 85–87, 2006.

[21] A. Carrasco-Casado, R. Vergaz, J. M. Sánchez-Pena, E. Otón, M. A. Geday, and J. M. Otén, "Low-impact air-to-ground free-space optical communication system design and first results," in *2011 International Conference on Space Optical Systems and Applications (ICSOS)*, pp. 109–112, 2011.

[22] L.-T. Le, H.-T. Le, J. Lee, H.-Y. Ma, and H.-Y. Lee, "Design of a society of automotive engineers regular curved retroreflector for enhancing optical efficiency and working area," *Crystals*, vol. 8, no. 12, 2018.

[23] V. S. Hsu, J. M. Kahn, and K. Pister, "Wireless communications for smart dust," Tech. Rep. UCB/ERL M98/2, EECS Department, University of California, Berkeley, 1998.

[24] S. Teramoto and T. Ohtsuki, “Optical wireless sensor network system using corner cube retroreflectors (CCRs),” in *IEEE Global Telecommunications Conference, 2004. GLOBECOM ’04.*, vol. 2, pp. 1035–1039 Vol.2, 2004.

[25] M. W. Khalid, R. Ahmed, A. K. Yetisen, and H. Butt, “Flexible corner cube retroreflector array for temperature and strain sensing,” *RSC Advances*, vol. 8, pp. 7588–7598, 2018.

[26] X. Xu, Y. Shen, J. Yang, C. Xu, G. Shen, G. Chen, and Y. Ni, “PassiveVLC: enabling practical visible light backscatter communication for battery-free IoT applications,” in *Proceedings of the 23rd Annual International Conference on Mobile Computing and Networking*, MobiCom ’17, (New York, NY, USA), pp. 180–192, Association for Computing Machinery, 2017.

[27] L. Janik, M. Novak, A. Dobesch, and L. Hudcova, “Retroreflective optical communication,” in *2017 Conference on Microwave Techniques (COMITE)*, pp. 1–4, 2017.

[28] A. V. Arecchi, T. Messadi, and R. J. Koshel, *Field Guide to Illumination*. USA: Society of Photo-Optical Instrumentation Engineers (SPIE), 2007.

[29] H. J. Eichler and O. Mehl, “Phase conjugate mirrors,” *Journal of Nonlinear Optical Physics and Materials*, vol. 10, pp. 43–52, 04 2012.

[30] J. Yun and B.-J. Jang, “Ambient light backscatter communication for IoT applications,” *Journal of electromagnetic engineering and science*, vol. 16, pp. 214–218, Oct. 2016.

[31] J. Li, A. Liu, G. Shen, L. Li, C. Sun, and F. Zhao, “Retro-VLC: Enabling battery-free duplex visible light communication for mobile and IoT applications,” in *Proceedings of the 16th International Workshop on Mobile Computing Systems and Applications*, HotMobile ’15, (New

York, NY, USA), pp. 21–26, Association for Computing Machinery, 2015.

[32] Z. Yang, Z. Wang, J. Zhang, C. Huang, and Q. Zhang, "Polarization-based visible light positioning," *IEEE Transactions on Mobile Computing*, vol. 18, no. 3, pp. 715–727, 2019.

[33] Y. Wu, P. Wang, K. Xu, L. Feng, and C. Xu, "Turboboosting visible light backscatter communication," in *Proceedings of the Annual Conference of the ACM Special Interest Group on Data Communication on the Applications, Technologies, Architectures, and Protocols for Computer Communication*, SIGCOMM '20, (New York, NY, USA), pp. 186–197, Association for Computing Machinery, 2020.

[34] P. Wang, Y. Wu, and C. Xu, "Poster: Polarization-based QAM for visible light backscatter communication," in *The 25th Annual International Conference on Mobile Computing and Networking*, MobiCom '19, (New York, NY, USA), Association for Computing Machinery, 2019.

[35] Z. Yang, Z. Wang, J. Zhang, C. Huang, and Q. Zhang, "Wearables can afford: Light-weight indoor positioning with visible light," in *Proceedings of the 13th Annual International Conference on Mobile Systems, Applications, and Services*, MobiSys '15, (New York, NY, USA), pp. 317—-330, Association for Computing Machinery, 2015.

[36] J.-M. Kim, S.-H. Lee, D.-H. Jeon, and S.-W. Lee, "Physical model of pixels in twisted nematic active-matrix liquid crystal displays," *IEEE Transactions on Electron Devices*, vol. 62, no. 10, pp. 3308–3313, 2015.

[37] Q. Wang, M. Zuniga, and D. Giustiniano, "Passive communication with ambient light," in *Proceedings of the 12th International on Conference on Emerging Networking EXperiments and Technologies*, CoNEXT '16, (New York, NY, USA), pp. 97–104, Association for Computing Machinery, 2016.

[38] R. Bloom, M. Zuniga, Q. Wang, and D. Giustiniano, "Tweeting with sunlight: Encoding data on mobile objects," in *IEEE INFOCOM 2019 - IEEE Conference on Computer Communications*, pp. 1324–1332, 2019.

[39] S. Shao, A. Khreishah, and H. Elgala, "Pixelated VLC-backscattering for self-charging indoor IoT devices," *IEEE Photonics Technology Letters*, vol. 29, no. 2, pp. 177–180, 2017.

[40] Y. Wu, P. Wang, and C. Xu, "Demo: Improving visible light backscatter communication with delayed superimposition modulation," in *The 25th Annual International Conference on Mobile Computing and Networking*, MobiCom '19, (New York, NY, USA), Association for Computing Machinery, 2019.

[41] R. Bloom, M. Z. n. Zamalloa, and C. Pai, "LuxLink: Creating a wireless link from ambient light," in *Proceedings of the 17th Conference on Embedded Networked Sensor Systems*, SenSys '19, (New York, NY, USA), p. 166–178, Association for Computing Machinery, 2019.

[42] S. K. Ghiasi, M. A. Z. n. Zamalloa, and K. Langendoen, "A principled design for passive light communication," in *Proceedings of the 27th Annual International Conference on Mobile Computing and Networking*, MobiCom '21, (New York, NY, USA), p. 121–133, Association for Computing Machinery, 2021.

[43] T. Xu, M. C. Tapia, and M. Zúñiga, "Exploiting digital micro-mirror devices for ambient light communication," in *19th USENIX Symposium on Networked Systems Design and Implementation (NSDI 22)*, (Renton, WA), pp. 387–400, USENIX Association, Apr. 2022.

[44] M. C. Tapia, T. Xu, Z. Wu, and M. Z. n. Zamalloa, "SunBox: Screen-to-camera communication with ambient light," *Proc. ACM Interact. Mob. Wearable Ubiquitous Technol.*, vol. 6, no. 2, 2022.

[45] P. Wang, L. Feng, G. Chen, C. Xu, Y. Wu, K. Xu, G. Shen, K. Du, G. Huang, and X. Liu, "Renovating road signs for infrastructure-to-

vehicle networking: A visible light backscatter communication and networking approach," in *Proceedings of the 26th Annual International Conference on Mobile Computing and Networking*, MobiCom '20, (New York, NY, USA), Association for Computing Machinery, 2020.

[46] S. Shao, A. Khreishah, and I. Khalil, "RETRO: Retroreflector based visible light indoor localization for real-time tracking of IoT devices," in *IEEE INFOCOM 2018 - IEEE Conference on Computer Communications*, pp. 1025–1033, 2018.

[47] S. Shao, A. Khreishah, and J. Paez, "PassiveRETRO: Enabling completely passive visible light localization for IoT applications," *Proceedings - IEEE INFOCOM*, vol. 2019-April, pp. 1540–1548, 2019.

[48] S. Shao, A. Khreishah, and I. Khalil, "Enabling real-time indoor tracking of IoT devices through visible light retroreflection," *IEEE Transactions on Mobile Computing*, vol. 19, no. 4, pp. 836–851, 2020.

[49] K. Xu, C. Gong, B. Liang, Y. Wu, B. Di, L. Song, and C. Xu, "Low-latency visible light backscatter networking with RetroMUMIMO," in *Proceedings of the 20th ACM Conference on Embedded Networked Sensor Systems*, SenSys '22, Association for Computing Machinery, 2022.

[50] W. Li, T. Chen, Z. Ou, X. Wen, Z. Xu, and C. Xu, "RetroFlex: enabling intuitive human-robot collaboration with flexible retroreflective tags," *CCF Transactions on Pervasive Computing and Interaction*, 2022.

[51] H. Wang, Z. Zhang, B. Zhu, J. Dang, L. Wu, L. Wang, K. Zhang, and Y. Zhang, "Performance of wireless optical communication with reconfigurable intelligent surfaces and random obstacles," 2020.

[52] J. J. P. Rodrigues, S. S. Compte, and I. de la Torra Diez, *e-Health SystemsTheory, Advances and Technical Applications*. Elsevier, 2016.

[53] Y. Yang, H. Wang, R. Jiang, X. Guo, J. Cheng, and Y. Chen, "A review of IoT-enabled mobile healthcare: Technologies, challenges, and future

trends," *IEEE Internet of Things Journal*, vol. 9, no. 12, pp. 9478–9502, 2022.

[54] O. Haddad, M.-A. Khalighi, S. Zvanovec, and M. Adel, "Channel characterization and modeling for optical wireless body-area networks," *IEEE Open Journal of the Communications Society*, vol. 1, pp. 760–776, 2020.

[55] W. Noonpakdee, "Indoor optical wireless communications employing corner cube retroreflector for health monitoring system," in *2013 Fifth International Conference on Ubiquitous and Future Networks (ICUFN)*, pp. 674–678, 2013.

[56] W. Noonpakdee, "Performance analysis of passive-active optical wireless transmission for personal health monitoring," in *2014 Sixth International Conference on Ubiquitous and Future Networks (ICUFN)*, pp. 17–21, 2014.

[57] W. Noonpakdee, "Hybrid passive-active optical wireless transmission for health monitoring system," *Wireless Personal Communications*, vol. 86, no. 4, pp. 1899–1911, 2016.

[58] H. B. Eldeeb, M. Elamassie, S. M. Sait, and M. Uysal, "Infrastructure-to-vehicle visible light communications: Channel modelling and performance analysis," *IEEE Transactions on Vehicular Technology*, vol. 71, no. 3, pp. 2240–2250, 2022.

[59] D. Darsena, G. Gelli, I. Iudice, and F. Verde, "Sensing technologies for crowd management, adaptation, and information dissemination in public transportation systems: A review," *IEEE Sensors Journal*, pp. 1–1, 2022.

[60] B. Ji, Y. Li, B. Zhou, C. Li, K. Song, and H. Wen, "Performance analysis of UAV relay assisted IoT communication network enhanced with energy harvesting," *IEEE Access*, vol. 7, pp. 38738–38747, 2019.

[61] H. Sahin and L. Guvenc, “Household robotics: autonomous devices for vacuuming and lawn mowing [applications of control],” *IEEE Control Systems Magazine*, vol. 27, no. 2, pp. 20–96, 2007.

[62] A. R. Al-Ali, I. A. Zualkernan, M. Rashid, R. Gupta, and M. Alikarar, “A smart home energy management system using IoT and big data analytics approach,” *IEEE Transactions on Consumer Electronics*, vol. 63, no. 4, pp. 426–434, 2017.

[63] Y. Song, F. R. Yu, L. Zhou, X. Yang, and Z. He, “Applications of the Internet of Things (IoT) in smart logistics: A comprehensive survey,” *IEEE Internet of Things Journal*, vol. 8, no. 6, pp. 4250–4274, 2021.

[64] Y. Liao, E. de Freitas Rocha Loures, and F. Deschamps, “Industrial Internet of Things: A systematic literature review and insights,” *IEEE Internet of Things Journal*, vol. 5, no. 6, pp. 4515–4525, 2018.

[65] Z. Ghassemlooy, W. Popoola, and S. Rajbhandari, *Optical Wireless Communications: System and Channel Modelling with MATLAB*. CRC Press, 2018.

[66] J. M. Kahn and J. R. Barry, “Wireless infrared communications,” *Proceedings of the IEEE*, vol. 85, no. 2, pp. 265–298, 1997.

[67] F. R. Gfeller and U. Bapst, “Wireless in-house data communication via diffuse infrared radiation,” *Proceedings of the IEEE*, vol. 67, no. 11, pp. 1474–1486, 1979.

[68] A. M. Street, P. N. Stavrinou, D. C. O’Brien, and D. J. Edwards, “Indoor optical wireless systems - a review,” *Optical and Quantum Electronics*, vol. 29, no. 3, p. 349–378, 1997.

[69] Z. Wang, Q. Wang, W. Huang, and Z. Xu, *Visible Light Communications: Modulation and Signal Processing*. IEEE Series on Digital & Mobile Communication, Wiley, 2017.

[70] D. Zwillinger, “Differential ppm has a higher throughput than ppm for the band-limited and average-power-limited optical channel,” *IEEE Transactions on Information Theory*, vol. 34, no. 5, pp. 1269–1273, 1988.

[71] Y. Xiang, M. Zhang, M. Kavehrad, M. I. S. Chowdhury, M. Liu, J. Wu, and X. Tang, “Human shadowing effect on indoor visible light communications channel characteristics,” *Optical Engineering*, vol. 53, no. 8, p. 086113, 2014.

[72] Z. Dong, T. Shang, Y. Gao, and Q. Li, “Study on vlc channel modeling under random shadowing,” *IEEE Photonics Journal*, vol. 9, no. 6, pp. 1–16, 2017.

[73] P. Chvojka, S. Vitek, S. Zvanovec, Z. Ghassemlooy, and S. Rajbhandari, “Analysis of nonline-of-sight visible light communications,” *Optical Engineering*, vol. 56, no. 11, p. 116116, 2017.

[74] S. T. Jovkova and M. Kavehard, “Multispot diffusing configuration for wireless infrared access,” *IEEE Transactions on Communications*, vol. 48, no. 6, pp. 970–978, 2000.

[75] J. B. Carruther and J. M. Kahn, “Angle diversity for nondirected wireless infrared communication,” *IEEE Transactions on Communications*, vol. 48, no. 6, pp. 960–969, 2000.

[76] J. M. Kahn, W. J. Krause, and J. B. Carruthers, “Experimental characterization of non-directed indoor infrared channels,” *IEEE Transactions on Communications*, vol. 43, no. 2/3/4, pp. 1613–1623, 1995.

[77] N. Hayasaka and T. Ito, “Channel modeling of nondirected wireless infrared indoor diffuse link,” *Electronics and Communications in Japan*, vol. 90, no. 6, pp. 9–19, 2007.

[78] V. Jungnickel, V. Pohl, S. Nonnig, and C. von Helmolt, “A physical model of the wireless infrared communication channel,” *IEEE Jour-*

nal on Selected Areas in Communications, vol. 20, no. 3, pp. 631–640, 2002.

[79] J. Chellam and R. K. Jeyachitra, “Energy-efficient bi-directional visible light communication using thin-film corner cube retroreflector for self-sustainable iot,” *IET Optoelectronics*, vol. 14, no. 5, pp. 223–233, 2020.

[80] M. H. Ullah, G. Gelli, and F. Verde, “Visible light backscattering communications in healthcare scenarios: Link modeling and performance analysis,” in *2022 IEEE International Conference on Internet of Things and Intelligence Systems (IoTaIS)*, pp. 179–185, 2022.

[81] B. T. Phong, “Illumination for computer generated pictures,” *Communications of the ACM*, vol. 18, pp. 311–317, 6 1975.

[82] C. Lomba, R. Valadas, and A. de Oliveira Duarte, “Experimental characterisation and modelling of the reflection of infrared signals on indoor surfaces,” *IEE Proceedings - Optoelectronics*, vol. 145, pp. 191–197(6), June 1998.

[83] Y. Wang, X.Wang, B. Zhu, Z. Shi, J. Yuan, X. Gao, Y. Liu, X. Sun, D. Li, and H. Amano, “Full-duplex light communication with a monolithic multicomponent system,” *Light Sci Appl*, vol. 83, pp. 1–7, 2018.

[84] A. J. C. Moreira, A. M. R. Tavares, R. T. Valadas, and A. M. Duarte, “Modulation methods for wireless infrared transmission systems: Performance under ambient light noise and interference,” in *SPIE Conference on Wireless Data Transmission*, pp. 226–237, 1995.

[85] A. J. C. Moreira, R. T. Valadas, and A. M. de Oliveira Duarte, “Optical interference produced by artificial light,” *Wireless Networks*, vol. 3, no. 2, pp. 131–140, 1997.

[86] A. J. C. Moreira, R. T. Valadas, and A. M. de Oliveira Duarte, “Performance of infrared transmission systems under ambient light interference,” *IEE Proc.-Optoelectronics*, vol. 143, no. 6, pp. 339–346, 1996.

[87] A. J. C. Moreira, R. T. Valadas, and A. M. de Oliveira Duarte, “Reducing the effects of artificial light interference in wireless infrared transmission systems,” in *IEE Colloquium on Optical Free Space Communication Links*, pp. 501–510, 1996.

[88] P. A. Hoeher, *Visible Light Communications: Theoretical and Practical Foundations*. Carl Hanser Verlag GmbH & Company KG, 2019.

[89] G. P. Agrawal, *Fiber-Optic Communication Systems*. Wiley Series in Microwave and Optical Engineering, Wiley, 2012.

[90] R. Ramaswami, K. Sivarajan, and G. Sasaki, *Optical Networks: A Practical Perspective*. Morgan Kaufmann series in networking, Elsevier Science, 2009.

[91] J. G. Proakis, *Digital communications (2nd ed.)*. McGraw-Hill, New York, 1989.

[92] Y. Liu, C. Yeh, C.-W. Chow, Y. Liu, Y. Liu, and H. Tsang, “Demonstration of bi-directional LED visible light communication using TDD traffic with mitigation of reflection interference,” *Optics express*, vol. 20, no. 21, pp. 23019–23024, 2012.

[93] Y. Wang, Y. Wang, N. Chi, J. Yu, and H. Shang, “Demonstration of 575-mb/s downlink and 225-mb/s uplink bi-directional scm-wdm visible light communication using rgb led and phosphor-based led,” *Optics express*, vol. 21, no. 1, pp. 1203–1208, 2013.

[94] G. Cossu, R. Corsini, and E. Ciaramella, “High-speed bi-directional optical wireless system in non-directed line-of-sight configuration,” *Journal of Lightwave Technology*, vol. 32, no. 10, pp. 2035–2040, 2014.

[95] O. Haddad and M. A. Khalighi, “Enabling communication technologies for medical wireless body-area networks,” in *2019 Global LIFI Congress (GLC)*, pp. 1–5, 2019.

[96] H. N. Qureshi, M. Manalastas, A. Ijaz, A. Imran, Y. Liu, and M. O. Al Kalaa, “Communication requirements in 5G-enabled healthcare applications: Review and considerations,” *Healthcare*, vol. 10, no. 2, 2022.

[97] Hamamatsu Photonics, “Silicon photodiodes.” https://www.hamamatsu.com/eu/en/product/optical-sensors/photodiodes/si-photodiodes.html, 2021.

[98] Thorlabs, “Optical filters.” https://www.thorlabs.com/newgrouppage9.cfm?objectgroup_id=145, 2021.

[99] Thorlabs, “Optics guide.” https://www.thorlabs.com/navigation.cfm?guide_id=21, 2021.

[100] I. S. Technologies, “Telecom filters.” https://www.iridian.ca/product-category/telecom-filters/, 2021.

[101] S. M. Kay, *Fundamentals of Statistical Signal Processing: Estimation Theory*. Upper Saddle River: Prentice-Hall, 1993.

[102] S. R. Teli, P. Chvojka, S. Vítek, S. Zvanovec, R. Perez-Jimenez, and Z. Ghassemlooy, “A SIMO hybrid visible-light communication system for optical IoT,” *IEEE Internet of Things Journal*, vol. 9, no. 5, pp. 3548–3558, 2022.

[103] G. Matta, R. Bahl, and M. Agarwal, “Capacity analysis of indoor visible light communication systems,” in *2019 Global LIFI Congress (GLC)*, pp. 1–4, 2019.

[104] L. Jia, F. Shu, N. Huang, M. Chen, and J. Wang, “Capacity and optimum signal constellations for VLC systems,” *Journal of Lightwave Technology*, vol. 38, no. 8, pp. 2180–2189, 2020.

[105] S. Ma, R. Yang, Y. He, S. Lu, F. Zhou, N. Al-Dhahir, and S. Li, “Achieving channel capacity of visible light communication,” *IEEE Systems Journal*, vol. 15, no. 2, pp. 1652–1663, 2021.

[106] R. Jiang, Z. Wang, Q. Wang, and L. Dai, “A tight upper bound on channel capacity for visible light communications,” *IEEE Communications Letters*, vol. 20, no. 1, pp. 97–100, 2016.

[107] J.-B. Wang, Q.-S. Hu, J. Wang, M. Chen, and J.-Y. Wang, “Tight bounds on channel capacity for dimmable visible light communications,” *Journal of Lightwave Technology*, vol. 31, no. 23, pp. 3771–3779, 2013.

[108] K. Xu, H.-Y. Yu, Y.-J. Zhu, and Y. Sun, “On the ergodic channel capacity for indoor visible light communication systems,” *IEEE Access*, vol. 5, pp. 833–841, 2017.

[109] D. H. Sliney and S. L. Trokel, *Safety Standards and Laser Exposure Limits*, pp. 87–97. New York, NY: Springer New York, 1993.

[110] A. Chaaban, Z. Rezki, and M.-S. Alouini, “On the capacity of intensity-modulation direct-detection Gaussian optical wireless communication channels: A tutorial,” *IEEE Communications Surveys and Tutorials*, vol. 24, no. 1, pp. 455–491, 2022.

[111] G. Abramovich and F. W. Wheeler, “LED eye safety considerations in the design of iris capture systems,” in *Sensing Technologies for Global Health, Military Medicine, Disaster Response, and Environmental Monitoring; and Biometric Technology for Human Identification VIII* (B. V. K. V. Kumar, S. Prabhakar, A. A. Ross, S. O. Southern, K. N. Montgomery, C. W. Taylor, and B. H. Weigl, eds.), vol. 8029, p. 80291X, International Society for Optics and Photonics, SPIE, 2011.

[112] N. L. Tsitsas and C. A. Valagiannopoulos, “Anomalous reflection of visible light by all-dielectric gradient metasurfaces [Invited],” *Journal of the Optical Society of America B*, vol. 34, pp. D1–D8, July 2017.

[113] R. A. Aoni, M. Rahmani, L. Xu, K. Zangeneh Kamali, A. Komar, J. Yan, D. Neshev, and A. E. Miroshnichenko, “High-efficiency visible light manipulation using dielectric metasurfaces,” *Scientific Reports*, vol. 9, no. 1, pp. 1–9, 2019.

[114] J. A. Dolan, H. Cai, L. Delalande, X. Li, A. B. F. Martinson, J. J. De Pablo, D. López, and P. F. Nealey, "Broadband liquid crystal tunable metasurfaces in the visible: Liquid crystal inhomogeneities across the metasurface parameter space," *American Chemical Society Photonics*, vol. 8, no. 2, pp. 567–575, 2021.

[115] A. R. Ndjiongue, T. M. N. Ngatched, O. A. Dobre, and H. Haas, "Towards the use of re-configurable intelligent surfaces in VLC systems: Beam steering," 2020.

[116] B. Cao, M. Chen, Z. Yang, M. Zhang, J. Zhao, and M. Chen, "Reflecting the light: Energy efficient visible light communication with reconfigurable intelligent surface," *IEEE Vehicular Technology Conference*, vol. 2020-November, 2020.

[117] J. Liu, M. Liu, Y. Bai, J. Zhang, H. Liu, and W. Zhu, "Recent progress in flexible wearable sensors for vital sign monitoring," *Sensors (Switzerland)*, vol. 20, no. 14, pp. 1–26, 2020.

[118] A. Arbabi, E. Arbabi, Y. Horie, S. M. Kamali, and A. Faraon, "Planar metasurface retroreflector," *Nature Photonics*, vol. 11, no. 7, pp. 415–420, 2017.

[119] M. Sun, X. Xu, X. W. Sun, X. Liang, V. Valuckas, Y. Zheng, R. Paniagua-Domínguez, and A. I. Kuznetsov, "Efficient visible light modulation based on electrically tunable all dielectric metasurfaces embedded in thin-layer nematic liquid crystals," *Scientific Reports*, vol. 9, no. 1, pp. 1–9, 2019.

[120] S. J. Kim, I. Kim, S. Choi, H. Yoon, C. Kim, Y. Lee, C. Choi, J. Son, Y. W. Lee, J. Rho, and B. Lee, "Reconfigurable all-dielectric Fano metasurfaces for strong full-space intensity modulation of visible light," *Nanoscale Horizons*, vol. 5, no. 7, pp. 1088–1095, 2020.

[121] J. Dai, J. Zhao, Q. Cheng, and T. J. Cui, “Independent control of harmonic amplitudes and phases via a time-domain digital coding metasurface,” *Light: Science and Applications volume*, vol. 7, no. 90, 2018.

[122] L. Zhang, X. Q. Chen, S. Liu, Q. Zhang, J. Zhao, J. Y. Dai, G. D. Bai, X. Wan, Q. Cheng, G. Castaldi, V. Galdi, and T. J. Cui, “Space-time-coding digital metasurfaces,” *Nature Communications*, vol. 9, no. 4334, 2018.

[123] L. E. M. Matheus, A. B. Vieira, L. F. M. Vieira, M. A. M. Vieira, and O. Gnawali, “Visible light communication: Concepts, applications and challenges,” *IEEE Communications Surveys and Tutorials*, vol. 21, no. 4, pp. 3204–3237, 2019.

[124] Q.-V. Pham, T. Huynh-The, M. Alazab, J. Zhao, and W.-J. Hwang, “Sum-rate maximization for UAV-assisted visible light communications using NOMA: Swarm intelligence meets machine learning,” *IEEE Internet of Things Journal*, vol. 7, no. 10, pp. 10375–10387, 2020.

[125] Y. Yang, Y. Yang, M. Chen, C. Feng, H. Xia, S. Cui, and H. V. Poor, “Joint LED selection and precoding optimization for multiple-user multiple-cell VLC systems,” *IEEE Internet of Things Journal*, vol. 9, no. 8, pp. 6003–6017, 2022.

[126] M. H. Khadr, I. Walter, H. Elgala, and S. Muhaidat, “Machine learning-based massive augmented spatial modulation (ASM) for IoT VLC systems,” *IEEE Communications Letters*, vol. 25, no. 2, pp. 494–498, 2021.

[127] R. Rishu, J. Kumud, and D. Abhishek, “Fairness enhancement of non-orthogonal multiple access in VLC-based IoT networks for intravehicular applications,” *IEEE Transactions on Vehicular Technology*, vol. 71, no. 7, pp. 7414–7427, 2022.

[128] D. Tse and P. Viswanath, *Fundamentals of Wireless Communication*. Cambridge Univ. Press, Cambridge, U.K., 2005.

[129] X. Huang, F. Yang, C. Pan, and J. Song, “Flexible NOMA-based NOHO-OFDM scheme for visible light communication with iterative interference cancellation,” *Optics Express*, vol. 29, pp. 5645–5657, Feb. 2021.